Texas A&M University
Mechanical Engineering Department
Turbomachinery Laboratory
Tribology Group

ROTORDYNAMIC PERFORMANCE OF A ROTOR SUPPORTED ON CARBON-GRAPHITE TILTING-PAD AIR BEARINGS

Research Progress Report to the TAMU Turbomachinery Research Consortium

TRC-B&C-01-16

by

Luis San Andrés
Mast-Childs Chair Professor
Principal Investigator

Yong Zheng
Research Assistant

May 2016

NOVEL CARBON-GRAPHITE GAS BEARINGS AND SEALS FOR TURBOMACHINERY
TRC PROJECT, TEES # 400124-00046

EXECUTIVE SUMMARY

ROTORDYNAMIC PERFORMANCE OF A ROTOR SUPPORTED ON CARBON-GRAPHITE TILTING-PAD AIR BEARINGS
TRC-B&C-01-16

LUIS SAN ANDRÉS, YONG ZHENG MAY 2016

High performance turbomachinery (TM), operating at high speeds, demands of stable operation and accurate position control to achieve higher power density. Oil free turbomachinery has a smaller foot-print with savings in weight and part count. Porous gas bearings (PGBs) are a promising technology, enabling oil free operation at high speeds and extreme temperatures with significant reduction in drag power loss and an increase in system efficiency. In particular, externally pressurized PGBs with tilting pads allow stable operation, offering high stiffness for enhanced load capacity and accurate positioning.

In 2015-2016, a series of measurements are conducted on a solid rigid rotor supported on a pair of tilting pad carbon-graphite porous gas bearings (CG-PGBs). Flow rate into the bearings is proportional to the supply pressure (P_s) for pressure ratio (supply pressure/ambient pressure) above 3.0, leading to an estimated permeability coefficient (κ) at ~1.2 x 10^{-15} m^2, on the low end of known porous media for bearing materials.

Rotor speed coast down tests from 8 krpm ($R_r \cdot \Omega_0$ = 42 m/s) show a deceleration driven mainly by the viscous drag in the porous bearings and lasting at least two minutes. Identified friction factor (f) of the bearings is as small as 0.03 for operation with the supply pressure of P_s at 5.84 bar. Increasing P_s to 7.77 bar further decreases f to 0.019, thus indicating a nearly friction free operation.

During imbalance tests, the rotor-bearing system crosses a critical speed at about 9 krpm. The rotordynamic measurements show the shaft motion is mainly synchronous and with amplitude steadily increasing with rotor speed as it approaches the critical speed. Most importantly, the amplitude of rotor response is proportional to the imbalance mass; hence demonstrating a linear behavior of the CG-PGBs supported rotor-bearing system.

Measurements of the shaft center displacement in vertical direction due to a static load applied by a hydrostatic (porous bearing) load mechanism leads to an estimation of the direct stiffness of the support bearings (K_{yy} ~ 19.7 MN/m), which is close in value to the bearings' direction stiffness obtained from impact load tests.

TABLE OF CONTENTS

NOMENCLATURE

C_b	Bearing radial clearance [mm]
C_θ	Viscous drag coefficient for porous bearings [N·m·s/rad]
D_b	Bearing diameter [mm]
D_r	Rotor diameter [mm], $D_r = 2R_r$
e	Radius of unbalance mass location [mm]
F_{DE}	Drive end bearing reaction force [N]
ΔF_{DE}	Increase in drive end bearing reaction force due to static load [N]
F_{NDE}	Non-drive end bearing reaction force [N]
ΔF_{NDE}	Increase in non-drive end bearing reaction force due to static load [N]
F_{shear}	Shear force [N]
F_{st}	Strain force measured by load cell [N]
F_{static}	Static load applied to the test rotor [N]
$f(P_s)$	Pressure force through a load pad [N]
f	Drag Friction factor [-]
G	Mass flow rate [kg/s]
H	Height of bearing pad [mm]
h	Gas film thickness [mm]
t	Pad thickness [mm], t_{max} = 9.1 mm, t_{min} = 2.2 mm
I_p, I_t	Polar and transverse mass moments of Inertia [kg·m^2]
K_{eff}	Effective stiffness coefficient [N/m]
κ	Permeability coefficients of porous material in radial direction [m^2]
L_b	Bearing pad axial length [mm]
L_r	Rotor length [mm]
M	Rotor mass [kg]
m	Mass imbalance [kg]
N_p	Bearing pad number [-], N_p = 5
p_r	Pressure ratio [-], P_s/P_a
P_a	Ambient pressure [Pa]
P_s	Air supply pressure [Pa]
$\Re$	Air gas constant [J/(kg·K)], $\Re$ =286.7 J/kg·K
R_p	Pad radius of curvature [mm]
R_r	Rotor radius [mm]
R_u	Radius of mass imbalance [mm]
T	Torque [N·m]
$T_{bearing}$	Shear drag of porous gas bearings [N·m]
T_{motor}	Drag torque of motor ball bearings [N·m]
T_s	Supplied air temperature [°C]
$T_{windage}$	Windage torque on the rotor surface [N·m]
$\tau_{r\theta}$	Shear stress [N/m^2]
τ	Time [s]
w	Pad width [mm]
W_r	Rotor weight [N]
W_L	Weight of load bar [N]
Ω	Rotor angular speed [rad/s], $\Omega_0 \sim$ maximum angular speed

θ_p	Bearing pad arc length [°]
ξ	Damping ratio [-]
ω_c	Critical speed [rad/s]
μ	Air absolute viscosity [Pa·s]
ρ	Air density [kg/m^3]

Abbreviations

DEH, DEV	Drive end bearing, horizontal and vertical directions
FBD	Free-body diagram
LBP	Load between pad
LPM	Liter per minute
MTM	Micro-turbomachinery
NDEH, NDEV	Free end bearing, horizontal and vertical directions
PGB	Porous gas bearing

LIST OF TABLES

LIST OF FIGURES

I. INTRODUCTION

Advancement in high performance turbomachinery (TM) imposes stringent requirements on efficiency, position control, reliability, as well as stable operation under extreme temperature conditions. Aerostatic gas bearings can help to achieve these goals, as they offer large centering stiffness and damping coefficients, as well as a high load capacity [1]. Further, gas bearings are inherently environment-friendly and contamination-free [1, 2].

Among externally pressurized gas bearings, a porous gas bearing (PGB) is an emerging alternative. A PGB comprises a layer of porous material as the bearing surface, through which, hydrostatic pressure pushes an even distribution of gas flow over the entire surface facing a rotor. This is a significant advantage against conventional orifice-fed gas bearings and leads to an increase in load capacity [3]. More benefits of PGBs include low heat generation and accordingly low thermal distortion of components, high stiffness for precise rotor motion control at high rotor speed, and avoidance of rotor rub during rotor start up and coast down [3, 4]. Further, PGBs are simple in construction and hence of low cost [5]. In particular, PGBs with a tilting-pad design further eliminates destabilizing cross-coupled stiffnesses, thus leading to a stable rotor-bearing system.

Recently, PGBs with a novel carbon-graphite matrix (CG-PGBs) have become commercially available with applications into medical imaging tomography machines, high-speed spindles, and coordinate measuring machines. Other applications include compressors, turbochargers, turbo expanders, etc.

This report presents measurements of the rotordynamic response of a rigid rotor supported on a pair of tilting-five-pad CG-PGBs. The report discusses the:

(a) Identification of the test rotor free-free mode shapes and natural frequencies.

(b) Measurement of air flow vs. supply pressure to estimate the bulk-permeability (κ) of a porous pad.

(c) Rotor speed coast down tests and estimation of bearing drag torque, a drag coefficient (C_θ), a friction factor (f), and a calculated air film thickness (h).

(d) Imbalance response tests by adding calibrated imbalance to an end cap, up to 10 krpm.

(e) Static load tests via a hydrostatic loading mechanism.

II. LITERATURE REVIEW

The first experiment on porous journal bearings by Montgomery *et al*. [6] in 1955 demonstrates the practicability of porous gas bearings (PGBs) by rotating a light shaft (9.5 mm in diameter, 246.7 g, specific load ~3 kPa) in a pair of bronze-sintered PGBs up to a speed of 250 krpm ($R_r \cdot \Omega_0$ = 124 m/s).

Since then, major efforts regarding PGBs have been towards the prediction of performance and rotordynamic analyses providing reference and design criteria for PGBs. Experimental results have been few and far in between.

Accounting for surface roughness, flow measurements through the porous bushings by Sneck *et al.* [7-8] in 1965 reveal that the flow regime is laminar. The performance of a PGB highly depends on the permeability of the porous material. Both test and analysis results indicate slightly decreasing flow rate with an increasing journal eccentricity (e), while the flow coefficient (permeability, κ) first decreases slightly with an increasing pressure ratio (supply pressure/ambient pressure, $p_r = P_s/P_a$) and becomes insensitive to p_r for a journal displacement < 60% of the clearance (C_r).

Analysis by Sneck *et al*. [9] (1967) shows a slight influence of shaft speed rotation on the bearing flow rate for operation with a small journal eccentricity ($e/C_r < 0.20$). However, at a larger journal eccentricity ($e/C_r > 0.20$), the flow rate with shaft rotation is lower than that of a bearing with a nonrotating rotor operating at an otherwise same pressure ratio. The reduction in flow rate increases as the journal eccentricity increases, up to nearly 20%. In addition, the load capacity increases nearly-linearly with the flow resistance ratio (axial flow resistance over radial flow resistance) for $e/C_r < 0.60$ for operation at high rotor speed.

Castelli *et al.* [10] (1979) show that PGBs, having a traditional bushing design, are able to carry static loads up to $W/(LD)$ = 300 kPa. The authors corroborate that the gas flow rate diminishes slightly as the journal eccentricity increases. The decrease in flow rate is lesser in bearings with a higher permeability coefficient (κ), nearly independent of rotor speed. The load capacity increases with rotor speed due to the hydrodynamic effect, which is higher when the journal eccentricity is highest and the supply pressure lowest. In fact, the hydrostatic effect dominates over the hydrodynamic one for operation at the highest supply pressure, whereas the hydrodynamic effect is more evident with bearings having a higher permeability. Similarly, an increase in rotor speed

results in an increased bearing stiffness, most appreciable at the lowest supply pressure. Most importantly, no test PGBs demonstrated a pneumatic hammer instability.

Advances in manufacturing technology have made porous gas bearings with a novel tilting-pad design and a carbon-graphite matrix (CG-PGBs) along the bearing surface available at a low cost. Recently, San Andrés *et al.* [11] in 2015 conduct rotor speed coast down tests on a rigid rotor motor (0.89 kg in mass and 28.5 mm in diameter) supported on a pair of three-tilting-pad CG-PGBs. The investigation shows that the rotor-bearing system has a large damping ratio ($\zeta = 0.172$) despite the low viscosity of the lubricant - air. The authors also show that the bearing drag friction coefficient, at a rotor speed of 10 krpm (peak surface speed ~ 82 m/s at 55 krpm), is as small as $f = 0.007$, indicating near friction-free operation. An increase in supply pressure further reduces f to 0.004, and results in a longer duration of the rotor speed coast down. In brief, the rotordynamic results indicate stable operation, i.e., without subsynchronous whirl, for all test conditions.

Next, this report presents the results and corresponding discussion of a series of rotordynamic tests performed on a solid rotor supported on tilting pad PGBs mounted in a load between pads (LBP) configuration. The results include: air flow measurements, rotor speed coast down tests, rotor imbalance response tests, and static load tests.

III. TEST RIG DESCRIPTION

Figure 1 displays a schematic view and a photograph of the test rig with the instrumentation setup. The solid steel rotor is 457 mm in length (L_r), 100 mm in outer diameter (D_r), and 285 N in weight (W_r). Two pedestals host a pair of tilting pad PGBs to support the rotor.

Table 1 presents the main parameters for the rotor and a bearing pad. Each gas bearing has a diameter (D_b) and axial length (L_b) of 100 mm and 73.1 mm, respectively.

A 3-phase AC motor (7.46 kW with maximum speed of 18 krpm) drives through a flexible quill shaft the rotor. A variable frequency drive (VFD) controls the rotational speed of the motor. An optical tachometer facing the quill shaft connecting the electric motor to the test rotor records the rotor speed and acts as a key-phasor for rotor displacements.

Table 1. Main parameters of rotor and carbon-graphite bearings.

Parts	Parameter	Symbol	Value	Unit
Rotor	Mass	M	29.12	kg
	Weight	W_r	285	N
	Specific load	$\frac{1}{2}W_r / (L_b D_r)$	19.5	kPa
	Diameter	D_r	100	mm
	Length	L_r	457	mm
Carbon-graphite bearing pad $N_p = 5$	Axial Length	L_b	73.1	mm
	Width	w	50.8	mm
	Radius	R_b	50	mm
	Arc length	θ_p	60	º
	Height	H	25.8	mm
	Pivot offset		50%	
	Pad preload		0	

Figure 2 presents the flow conduits for the supply of air into the bearings located at the rotor drive end (DE) and rotor non-drive end (NDE), as well as the supply of clean air into the hydrostatic load mechanism. Before entering the bearing pads, a series of filters remove first particles, then oil, and last humidity from the flowing air. Two flow meters (max. 50 liter/min) record the supplied air flow rate into each bearing at standard conditions (1 bar, 21 °C).

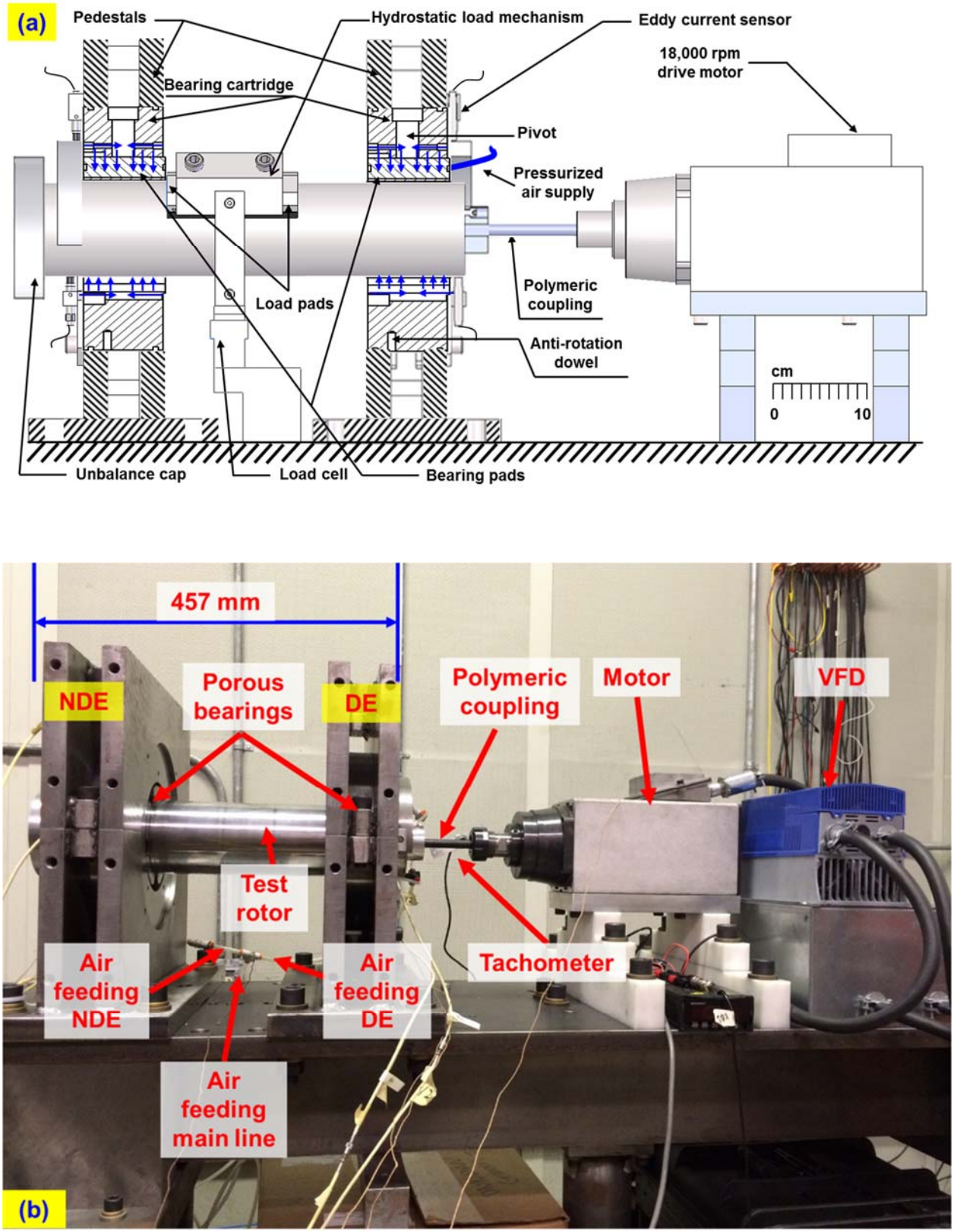

Figure 1. Test rig with a solid rotor supported on five-pad porous type gas bearings: (a) schematic view of test rig and (b) photograph of test rig with components labeled.

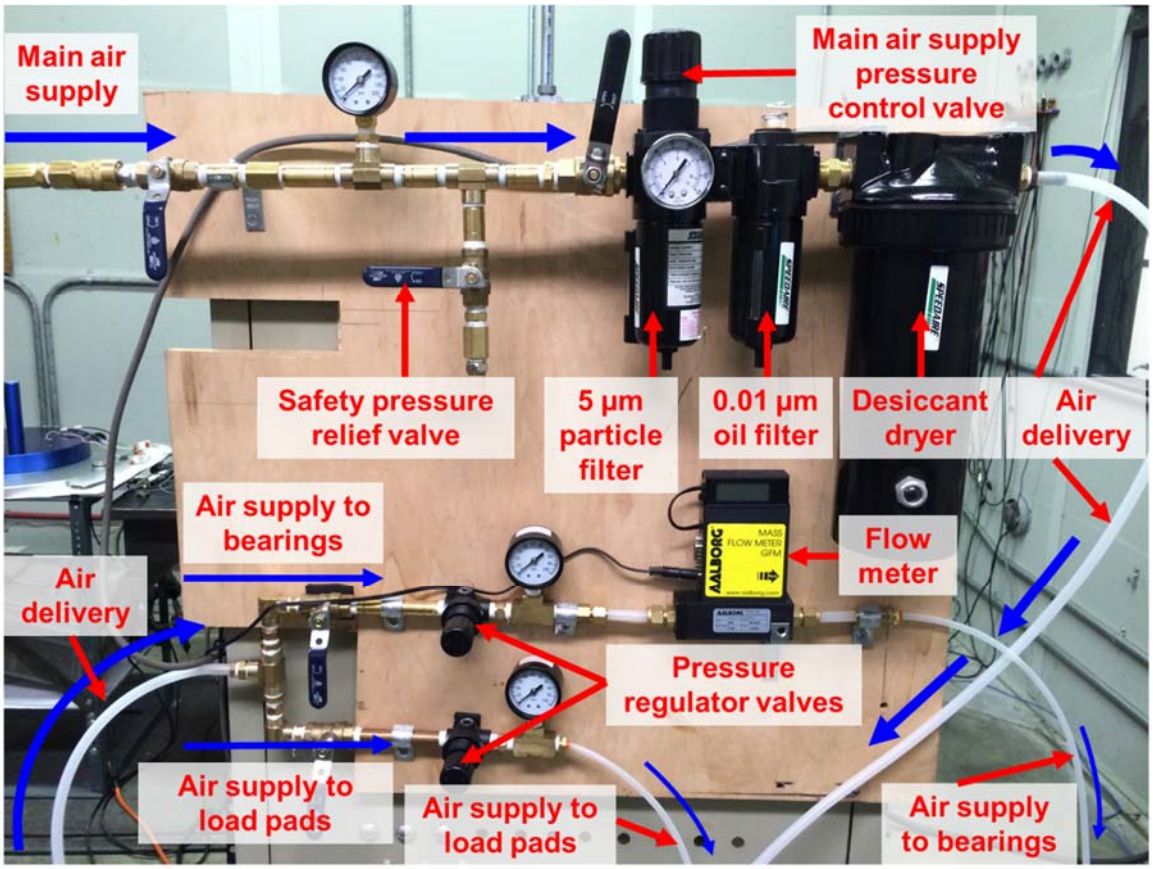

Figure 2. Photograph of airflow conduits with components labeled.

Figure 3 shows a close up view of the instrumentation setup for the rotor motion measurement at the drive end (DE) and non-drive end (NDE) bearings. Two pairs of orthogonally positioned eddy current sensors located at the rotor DE and rotor NDE measure the lateral rotor motions in the horizontal and vertical directions, respectively.

Figure 4(a) depicts a schematic view of a bearing installed in its cartridge and supporting the rotor under a load-between-pads (LBP) configuration. Each bearing has five pads with arc length of 60° and 50% pivot offset, recall Table. 1. Two thermocouples measure the pad cartridge temperature of the bottom (loaded) pads. Figure 4(b) portrays an isometric view of the bearing. At the end of the connecting stem, each bearing pad rests on a pivot that imposes no resistance against tilting motion, allowing the pad to tilt in both circumferential and axial directions. The threaded stem connects the bearing pad to the pedestal via a washer with adjustable mechanical preload, to render no clearance between the pad and rotor. Figure 4(c) shows a top view of the pad surface and a lateral view of the pad end, as well as the location on the pad cartridge for a thermocouple.

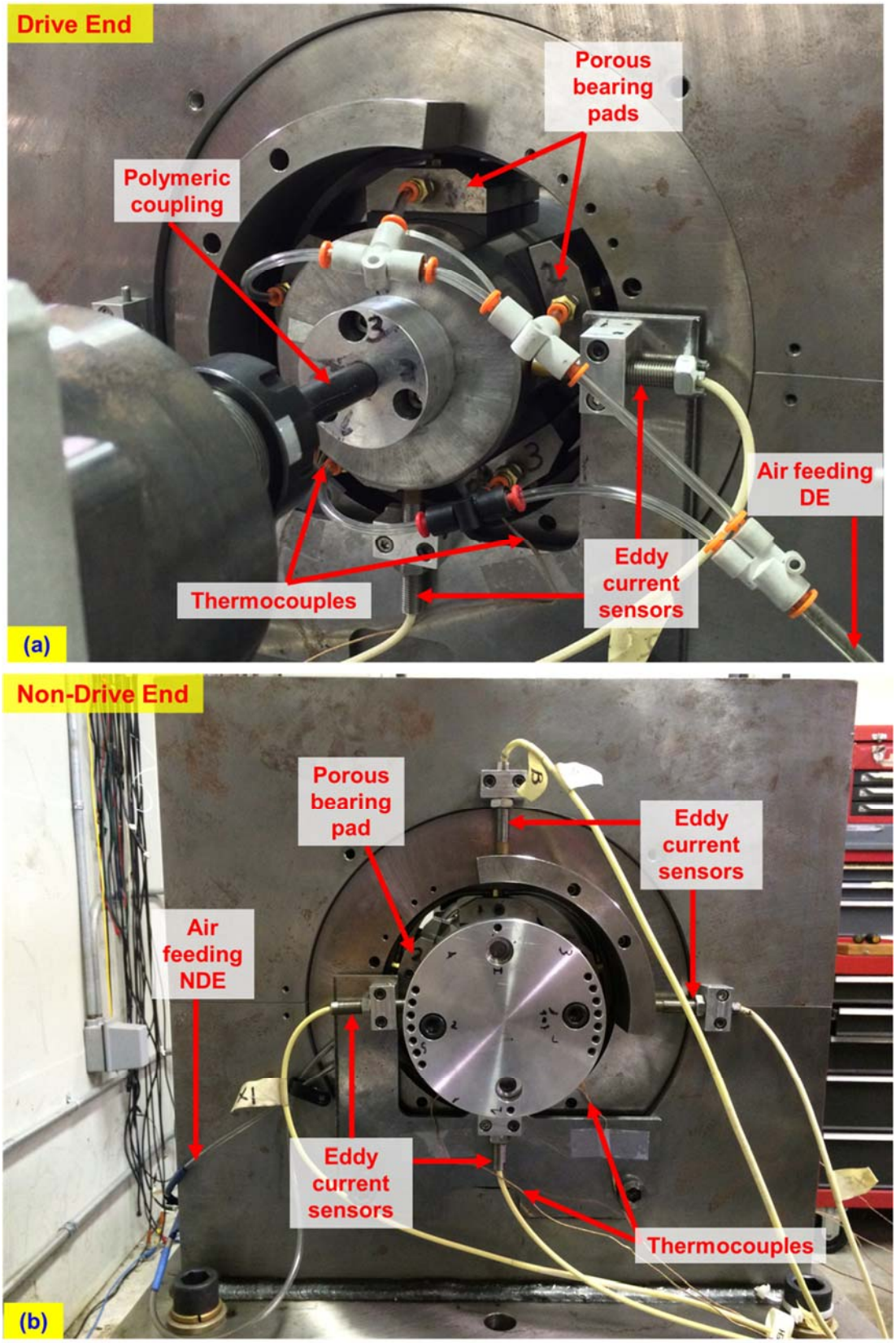

Figure 3. Instrumentation setup on rotor (a) drive end and (b) non-drive end bearings.

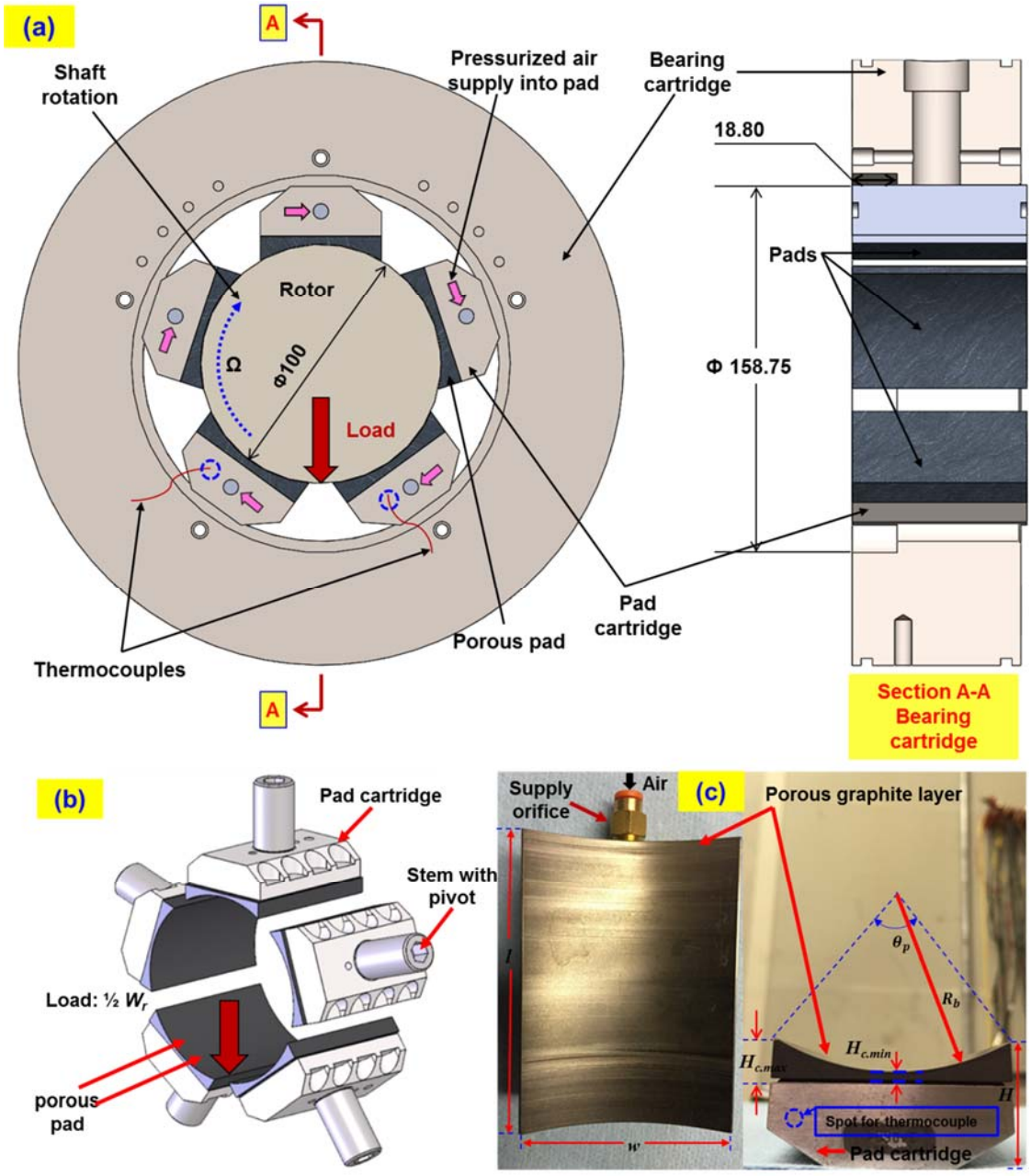

Figure 4. Photographs of a 5-pad porous type tilting-pad bearing including (a) schematic view of a bearing installed in its cartridge, (b) isometric view of a bearing and (c) top and side views of a bearing pad. t_{max} = 9.1 mm, t_{min} = 2.2 mm.

Six K-type thermocouples measure the temperature at various locations including: the motor surface, the main line of the air supply, pad base of two bottom (loaded) bearing pads at the rotor DE and NDE, respectively.

A commercial data acquisition system records displacements measured by the eddy current sensors, as well as the rotor speed that also serves as a key phasor. Two oscilloscopes display the

shaft orbits at the DE and NDE bearing locations, respectively. A multi-channel digital displayer shows the temperature measured by the six K-type thermocouples.

Appendix A [12] lists the physical rotor mass properties, as well as the rotor free-free mode shapes and natural frequencies. These natural frequencies are well above the motor operation speed range (max. ~ 18 krpm), hence qualifying the test shaft as a rigid rotor.

IV. EXPERIMENTAL PROCEDURE AND TEST RESULTS[1]

AIR FLOW THROUGH POROUS BEARINGS

This section presents measurements of the mass flow versus supply pressure with air at ambient temperature (~ 21° C). Two mass flow meters, each installed in distinct supply lines, display the flow, while separate regulator valves set the supply pressure (P_s) before gas passes through the meters. Note that the small pressure drop downstream of the meters (losses in the tubing and orifices) is not accounted for.

To determine if the rotor brings in a significant flow resistance, the tests are conducted w/o the rotor in place, and the flow meter records the flow rate into each bearing. For each set up, each bearing undergoes two sets of measurements, one with the supply pressure increasing from the ambient pressure to a maximum of 7.77 bar ($P_{s,max,}$ ~ 98 psig) and the other with the supply pressure decreasing from $P_{s,max}$ to ambient.

Without the rotor in place, Figure 5 depicts the recorded mass flow[2] (G) into both the DE and NDE bearings versus the pressure ratio ($p_r = P_s / P_a$). The supply pressure (P_s) increases from ambient (1 bar) to a maximum (7.77 bar) then decreases to ambient. For a low supply pressure, < 4.4 bar, the flow to both bearings grows non-linearly as P_s increases. For a higher supply pressure, the flow transitions to linear, likely due to air choking. Both bearings show dissimilar flow, albeit with a maximum ~10% variation at the highest supply pressure. The difference is ascribed to the dissimilar pads' surface condition on each, some pads show distinctive (minor) wear. Incidentally, the measured flow is indifferent to the process of pressurization or depressurization. Note that the flow meter uncertainty U_V and the pressure gauge uncertainty U_{Ps} are 0.75 liter per minute (LPM) and 2%, respectively.

[1] Significant portion of this section reproduces ad-verbatim material in Ref. [13]
[2] The mass flow (G) refers to the amount of gas flowing into the five pads for each bearing, DE or NDE.

According to Forchheimer's law [14], the pressure drop through a porous material is due to both diffusion and inertial effects. With the inertial effect neglected and the rotor in place, Darcy's law states the relationship between the pressure drop (ΔP) through a porous media with thickness (t) as:

$$\frac{\Delta P}{t} = \frac{\mu v}{\kappa} \tag{1}$$

where μ = 19.8 ×10^{-6} Pa·s is the air viscosity at T = 294 K, v is the average gas velocity, and κ is a permeability coefficient.

The gas velocity $v = G/(\rho A_{pad})$ with G as the mass flow rate and $A_{pad} = (l \cdot \theta \cdot R_b)$ is the area of a single pad surface. Above ρ is an average gas density across the porous material $\rho = \frac{1}{2}(P_s + P_a)/(\Re T)$. Rearranging Eq. (1), an equivalent κ for the whole bearing is

$$\kappa = \frac{\mu t}{N_{pad} A_{pad}} \frac{G \Re T}{\frac{1}{2}\left(P_s^2 - P_a^2\right)} \tag{2}$$

where $\Re$ = 286.7 J/kg·K is the gas constant for air and N_{pad} = 5.

With the rotor in place but without rotation, Figure 6 presents the measured flow rate into the DE and NDE bearings versus pressure ratio ($p_r = P_s/P_a$). The flow rate trends with the rotor in place are similar to those in Figure 5 without the rotor in place, albeit with slightly lower magnitude, as shown in Figure 7 that compares the flows with and without the rotor in place. With the rotor in place, the flow rate into DE bearing decreases by 7% to 15% as the supply pressure grows above 3 bar. The air gap between the bearing pads and the rotor acts as an additional restriction, alas not effective to reduce the flow of air. The flow rate into NDE bearing displays a similar behavior. Note that the actual clearance of the rotor with its bearing pads is unknown.

As a description of behavior, from null to a low supply pressure (< 3 bar), the rotor rests on the bottom two pads and there is a small clearance at the top pads where air escapes. When the supply pressure reaches ~3 bar, the rotor lifts and can be spun by hand, though occasionally contacting the bottom pads. At a supply pressure of 4.4 bar, the rotor floats on the bearings and is nearly friction free. The flow into the DE bearing at the maximum supply pressure (~7.77 bar) reaches a maximum of 0.93 g/s [46.5 LPM], in contrast to the "without rotor" condition ~ 0.98 g/s [48.5 LPM] at 7.77 bar (see Figure 7).

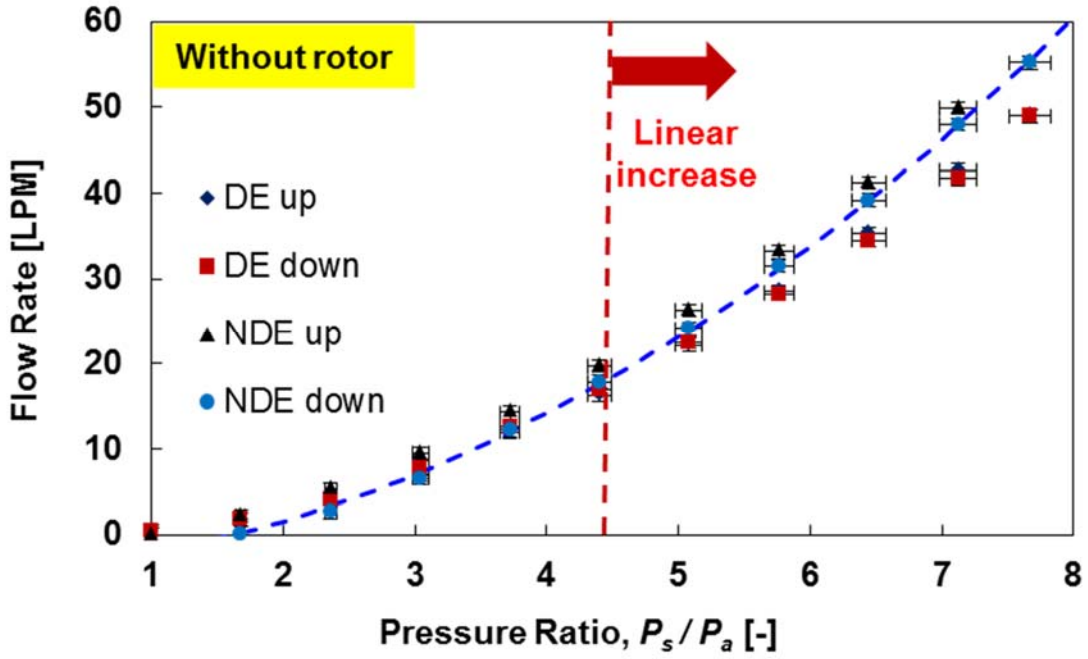

Figure 5. Measured flow rate into drive end and non-drive end bearings versus pressure ratio ($p_r = P_s/P_a$). Without rotor. Supply pressure (P_s) increases from ambient to 7.77 bar (abs) and then decreases to ambient. T_s = 21 °C. Flow rate uncertainty: 0.75 LPM. Pressure gauge uncertainty: 2%.

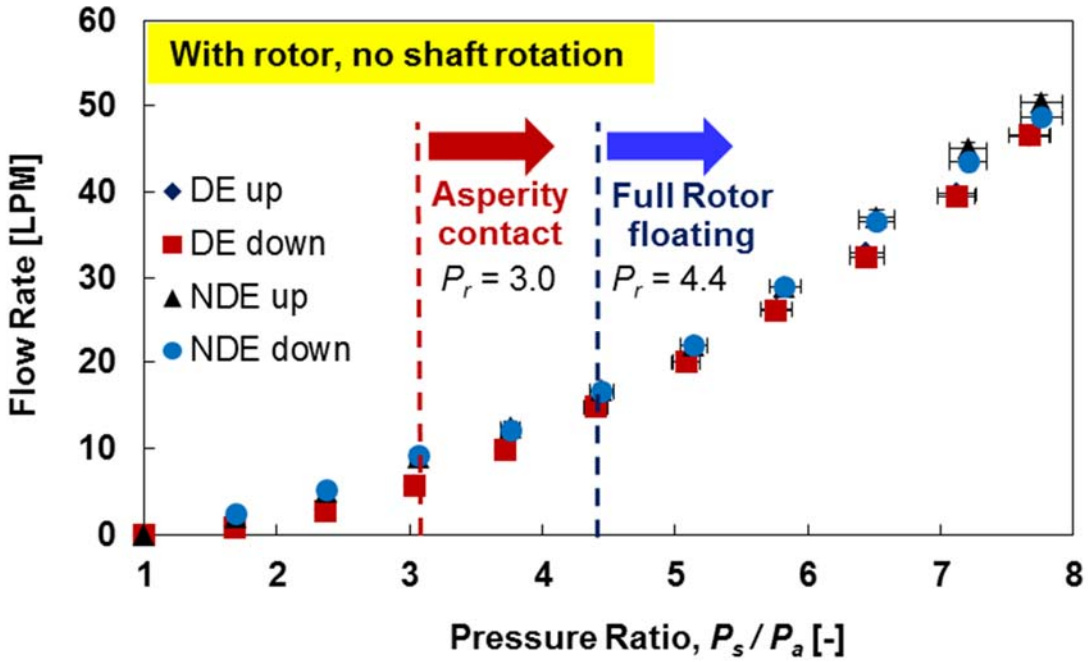

Figure 6. Measured flow rate into drive end and non-drive end gas bearings versus pressure ratio ($p_r = P_s/P_a$). Rotor installed and supported by bearings. No shaft rotation. Supply pressure (P_s) increases. T_s = 21 °C. Flow rate uncertainty: 0.75 LPM. Pressure gauge uncertainty: 2%.

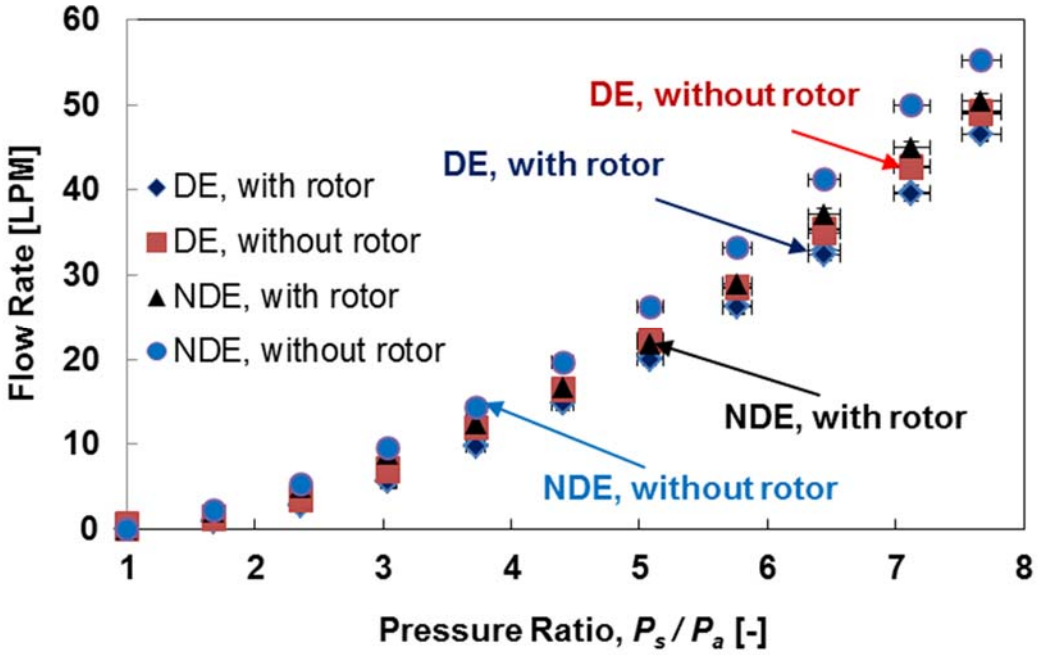

Figure 7. Comparison of measured flow rate into bearings with and without rotor in place. Drive end and non-drive end. No shaft rotation. T_s = 21 °C. Flow rate uncertainty: 0.75 LPM. Pressure gauge uncertainty: 2%.

Figure 8 depicts the estimated permeability coefficient (κ) versus pressure drop ($\Delta P = P_s - P_a$) for both DE and NDE bearings. For the whole range of ΔP, κ keeps almost constant for both bearings, but decreases slightly for the NDE bearing and is on the low end of other magnitudes reported in the literature for porous graphite bearings, that is κ $\{10^{-16}$ m^2 - 10^{-10} m$^2\}$ as per Refs. [15, 16]. For the lowest supply pressure, there is a noticeable difference in κ between both bearings, pointing to the difference in surface condition. One of the bearings (DE) seized the rotor while spinning at a high speed (9 krpm). Nonetheless, DE and NDE bearings are generally close to each other in the magnitude of κ, with the difference in κ converging as the supply pressure increases. This variation is probably due to slight distortions of the porous material at higher-pressure differences, which results in a very small decrease in the hydraulic clearance. However, the permeability of both bearings reaches 1.2 x 10^{-15} m^2 as the supply pressure increases (flow rate does too).

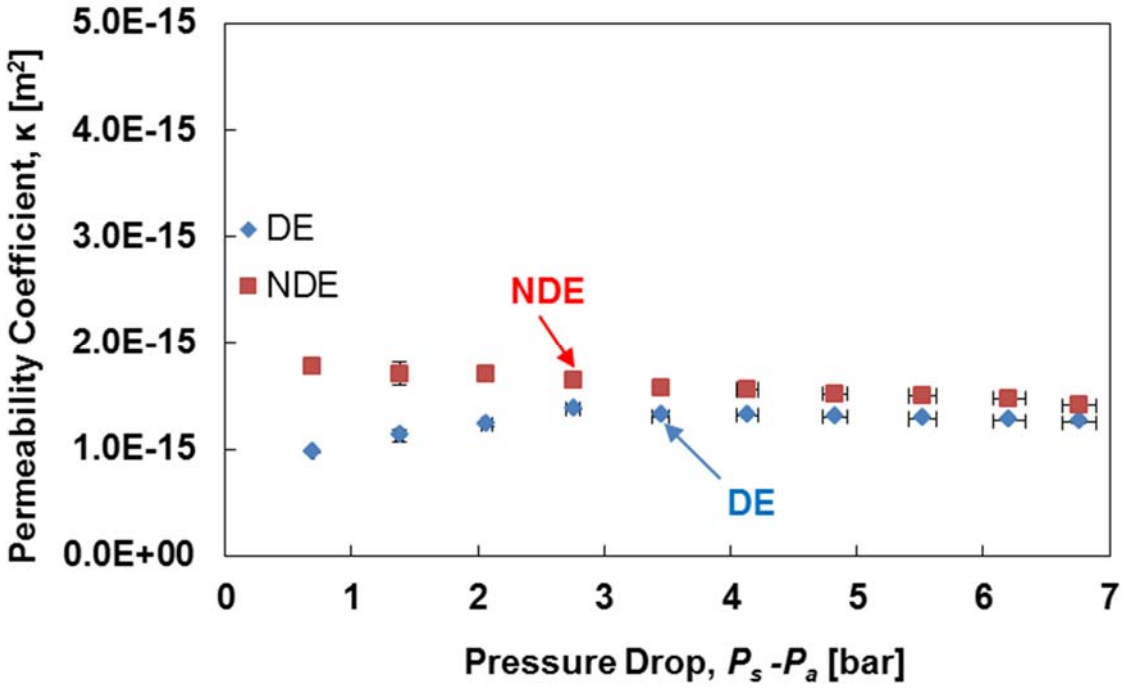

Figure 8. Estimated permeability coefficient (κ) versus pressure drop ($P_s - P_a$). No shaft rotation. Drive end (DE) and non-drive end (NDE) bearings.

ROTOR SPEED COAST DOWN TESTS

With the air supply, the motor drives the balanced test rotor up to 8 krpm (surface speed $R_r \cdot \Omega_0$ = 42 m/s) then a safety switch turns off the power to the motor and enables a speed coast down of the spinning rotor [11]. The elapsed time required for the rotor to come to rest from the peak speed determines the time constant of the system, from which an estimated drag torque is available. During the test, the tachometer measures the rotor speed, while the two pairs of eddy current sensors measure the rotor lateral displacements along the horizontal and vertical directions. Note that in the rotor speed coast down tests, the rotor is not intentionally imbalanced. The data-acquisition system records the data with the bearings supplied with air pressure P_s = 5.84, 6.53, 7.22 and 7.77 bar (absolute), respectively, cold at T = 294 K.

Once the motor is disconnected from the power source, the rotor decelerates and comes to rest mainly due to the shear drag of the porous gas bearings ($T_{bearing}$), the drag of the motor ball bearings (T_{motor}), and the windage torque on the rotor surface ($T_{windage}$) [15]:

$$I_P \frac{\partial \Omega}{\partial t} + 2T_{bearing} + T_{motor} + T_{windage} = 0 \qquad (3)$$

where $I_p = 0.038$ kg·m^2 is the polar mass moment of inertia for the coupled rotor and motor. The viscous drag torque from the air bearings is viscous in character and proportional to the rotor speeds:

$$T_{bearing} = C_\theta \Omega \tag{4}$$

where C_θ is a shear rotational drag coefficient (κ), and Ω is the rotor angular speed (rad/s). The break-away torque from the motor ball bearings is measured with a calibrated torque screwdriver, as shown in Figure 9, inserted in the coupling hole. With the test rotor disconnected from the motor, the torque measurement indicates a constant magnitude $T_{motor} = 0.028$ N·m.

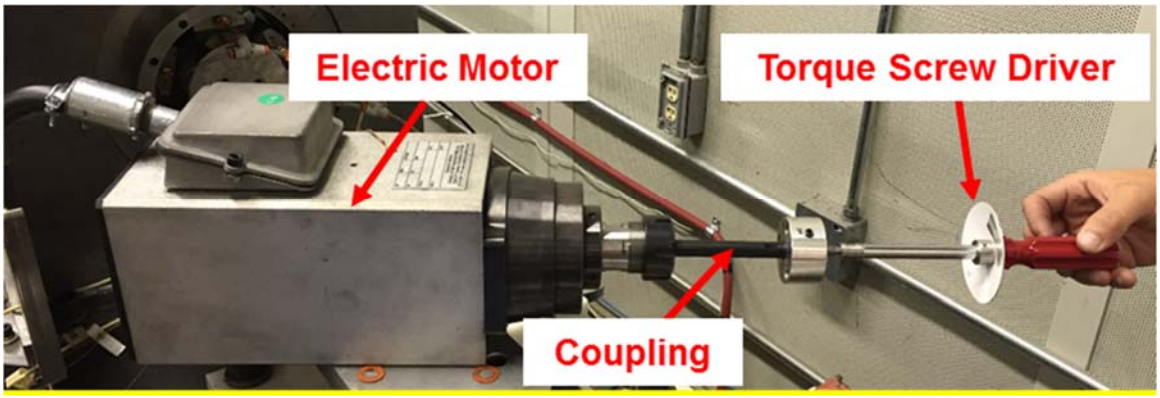

Figure 9. Measurement of ball bearing torque with a calibrated torque screwdriver.

Figure 10 shows the rotor speed ratio (Ω/Ω_0) versus time for coast down speed tests under various supply pressure. At each of the supply pressure conditions, the initial rotor deceleration is linear in the logarithmic scale, thus indicating viscous drag from the bearings and not windage on the rotor (~Ω^2). Note that an increase in the supply pressure results in a longer duration of the rotor deceleration. Tests with $P_s = 6.53$, 7.22 and 7.77 bar evidence little difference in the deceleration rate. As P_s decreases to 5.84 bar the increase in drag from the porous bearings becomes apparent. For $\Omega/\Omega_0 < 0.2$ and under all supply pressure conditions, the rotor speed decelerates rather rapidly as it starts contacting the bearing pads (rubbing).

Ref. [15] indicates that windage losses are important for rotors operating with large surface speeds or within a tight annular gap. In the current tests, the rotor does not operate within an enclosure or at a large surface speed ($R_r \cdot \Omega_0 < 42$ m/s); hence, as evidenced by the rotor speed decay data, the windage loss on the rotor surface is likely small ($T_{windage} \sim 0$ N·m).

At the lowest supply pressure (5.84 bar), the temperature of the loaded pads increases[3] (~5 °C) as the rotor accelerates from rest to 8 krpm. The excessive amplitude of rotor motion and local increase in pad temperature are a concern. If not carefully monitored, excessive rotor displacements and rotor material growth could lead easily to rotor seizure on its bearings, as discussed in a following section.

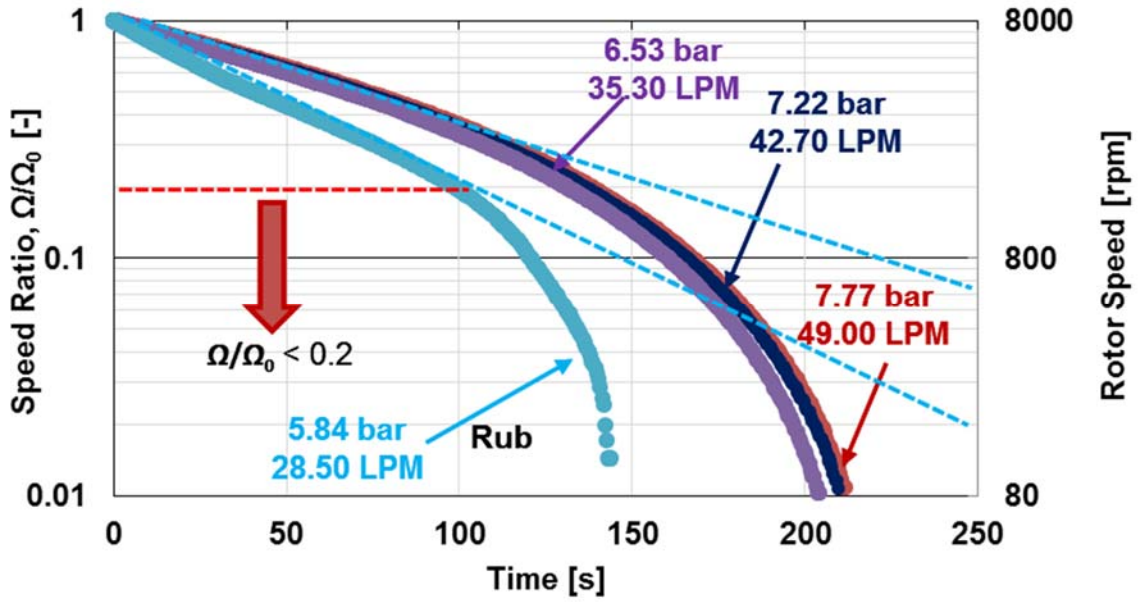

Figure 10. Recorded rotor speed ratio (Ω/Ω_0) vs. deceleration time for operation with P_s = 5.84, 6.53, 7.22 and 7.77 bar (abs). Rotor deceleration from 8 krpm, ω = 838 rad/s.

Table 2 includes the calculated viscous drag torque $T_{Bearing}=C_\theta \Omega_0$ for one of the air bearings, and which is much larger than the break-away drag torque in the motor ball bearings (0.028 N·m). The friction factor (f) for one bearing follows as [11]:

$$f = T_{bearing} / (\frac{1}{2} W_r R_b) \tag{5}$$

Table 2 also presents the bearing drag coefficient (C_θ) extracted from the rotor deceleration measurements for operation at increasing supply pressure. Note that for time τ >100 s, the rotor decelerates more rapidly, indicating an additional resistance adding to the viscous drag. In this region, the bearings operate under a mixed-lubrication regime, asperity contact.

[3] For 6.53-7.77 bar supply pressure, the temperature in the loaded pads (DE and NDE) did not increase more than 1 °C during the rotor acceleration/deceleration tests.

The magnitudes listed in Table 2 demonstrate the rotor operates with very little drag. Incidentally, for a uniform gas film thickness (h) in all the pads, the drag torque and accordingly an effective gas film thickness (h) are easily modeled as [11]

$$T_{bearing} = C_\theta \Omega = \mu \frac{\Omega}{h} L_b \theta_P R_b^3 N_{pad} \tag{6}$$

and

$$h = N_{pad} \mu L_b R_b^{\ 3} \theta_p / C_\theta \tag{7}$$

Figure 11 depicts the trend of the estimated effective gas film thickness (h) as the supply pressure (P_s) into bearings increases from 5.84 to 7.77 bar. At first, increase in P_s results in significant increase in the gas film thickness. However, further increase in P_s leads to slight increase in h.

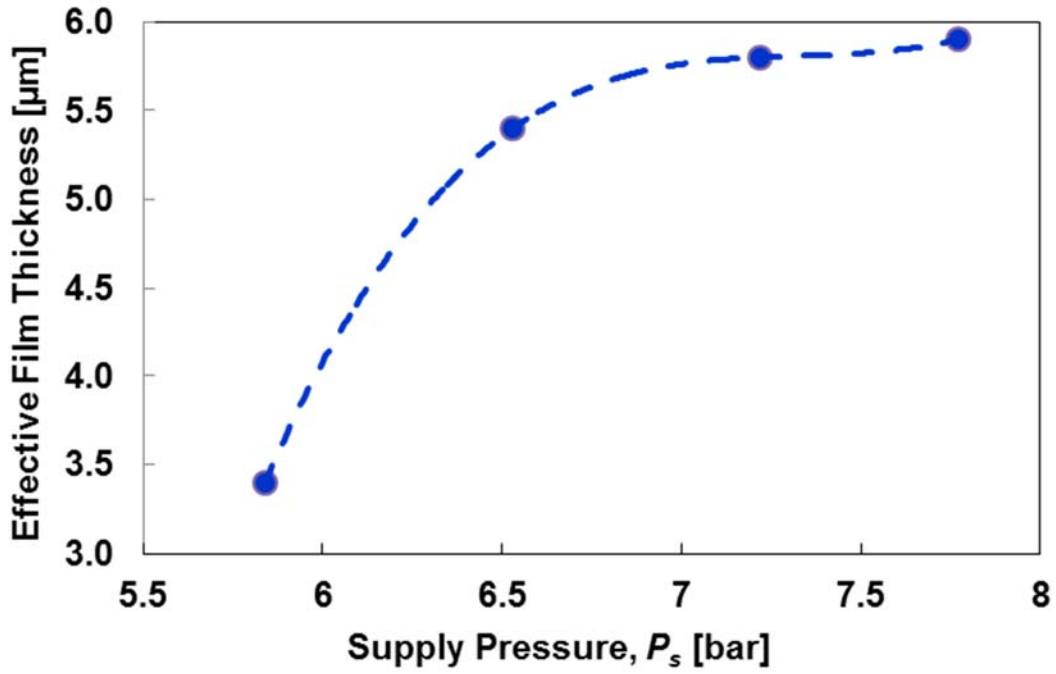

Figure 11. Effective gas film thickness vs. supply pressure. Ps = 5.84, 6.53, 7.22 and 7.77 bar (abs). Rotor deceleration from 8 krpm, ω = 838 rad/s.

Table 2 also contains an estimation of the air gap (h), just a few micrometer, increasing with the gas supply pressure. Note that the parameters calculated are estimates that disregard non-viscous effects.

Table 2. Gas bearing drag torque ($T_{bearing}$), rotational drag coefficient (C_θ), friction factor (f) and air film thickness (h) estimated from rotor free coast down tests. Operation with increasing supply pressure.

Air supply pressure P_s [bar, abs]	$T_{bearing}$ at 8 krpm [N·m]	C_θ, [10^{-3} N·m·s/rad]	Friction factor, f [-]	Effective Film thickness, h [μm]
5.84	0.230±0.014	0.275±0.005	0.033±0.006	3.4±1
6.53	0.147±0.002	0.176±0.002	0.021±0.002	5.4±1
7.22	0.138±0.003	0.165±0.002	0.020±0.003	5.8±1
7.77	0.134±0.003	0.160±0.014	0.019±0.003	5.9±1

IMBALANCE RESPONSE TESTS

This section presents measurements of the rotor dynamic response due to calibrated mass imbalances (m) inserted at radius e = 54 mm. The tests were conducted with gas supplied at P_s = 5.84, 6.53, and 7.77 bar (absolute) into the DE and NDE bearings.

Figure 12 (a) and Figure 12 (b) display an end cap, bolted to the NDE of the rotor, to insert calibrated masses. The cap has a total of 14 holes, 7 and 7, 180° apart. Figure 12(c) depicts the test rotor with an added mass (imbalance) inserted in a hole of the end cap.

The same procedure for the rotor speed coast down tests applies here regarding the rotor while accelerating and decelerating.

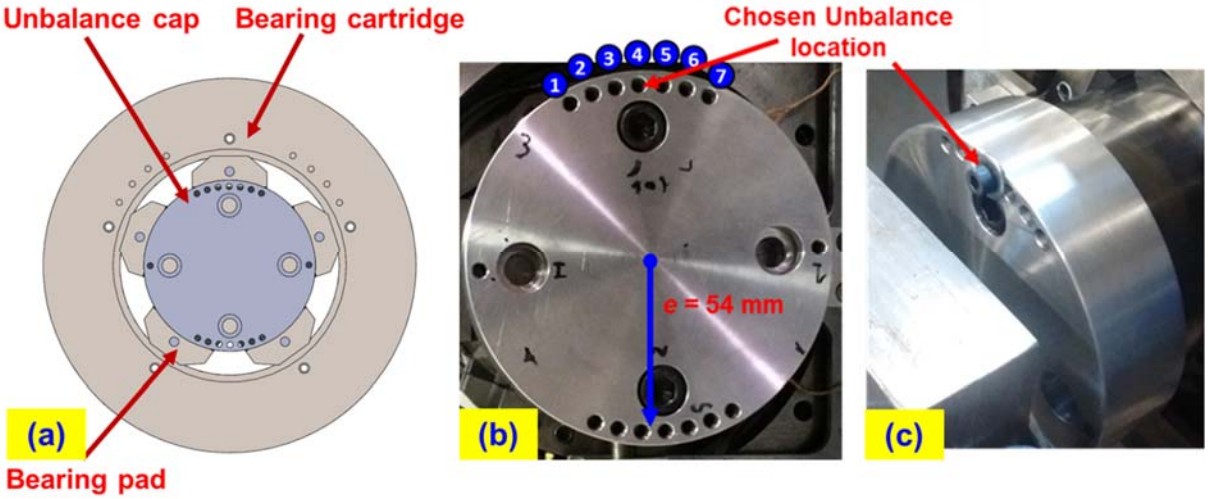

Figure 12. Rotor end cap with holes for insertion of imbalances.

The added masses are m_1 = 3.45 g, m_2 = 4.20 g and m_3 = 6.90 g, and which act as a periodic excitation ($m \cdot e \cdot \Omega^2$) of the test rotor. The rotor off-center mass displacement $u = m \cdot e/M$ equals 6.7,

8.1, and 13.3 g·mm/kg for each added imbalance, respectively. As per ISO 1940-1 [18], these u's lead to a balancing grade G > 2.5 ($u_{G=2.5}$ = 2.6 g·mm/kg) for operation at 10 krpm. That is, the mass imbalances applied exceed those in accepted practice.

Figure 13 and Figure 14 present the waterfall plots of the baseline rotor speed coast down response at NDE bearing along the horizontal and vertical directions, respectively. Note the low magnitudes of super synchronous frequency motions compared to those at synchronous speed, as well as the absence of any subsynchronous motions.

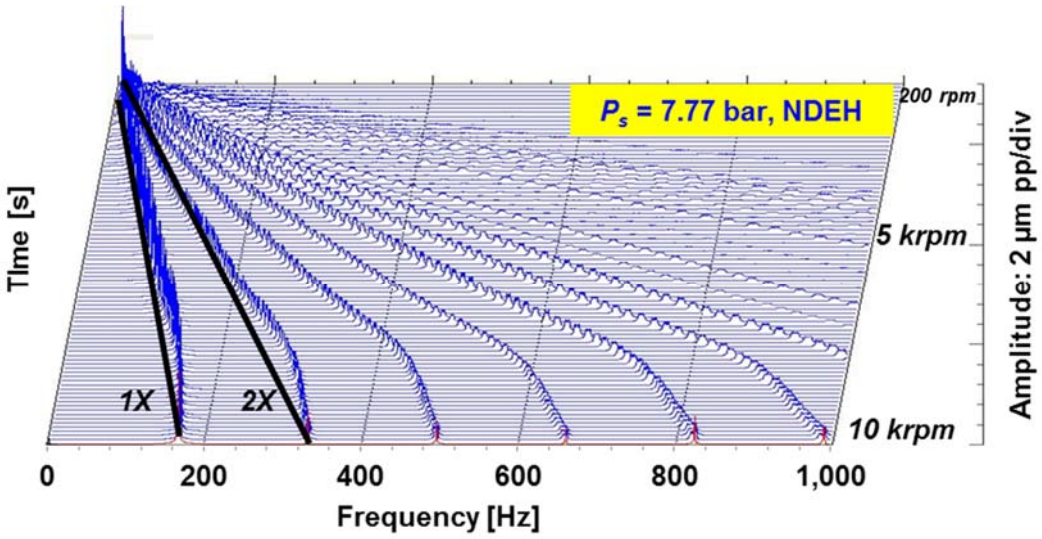

Figure 13. Waterfall plot of baseline rotor coast down response at drive end, horizontal plane (DEH). P_s = 7.77 bar, T_s = 21 °C.

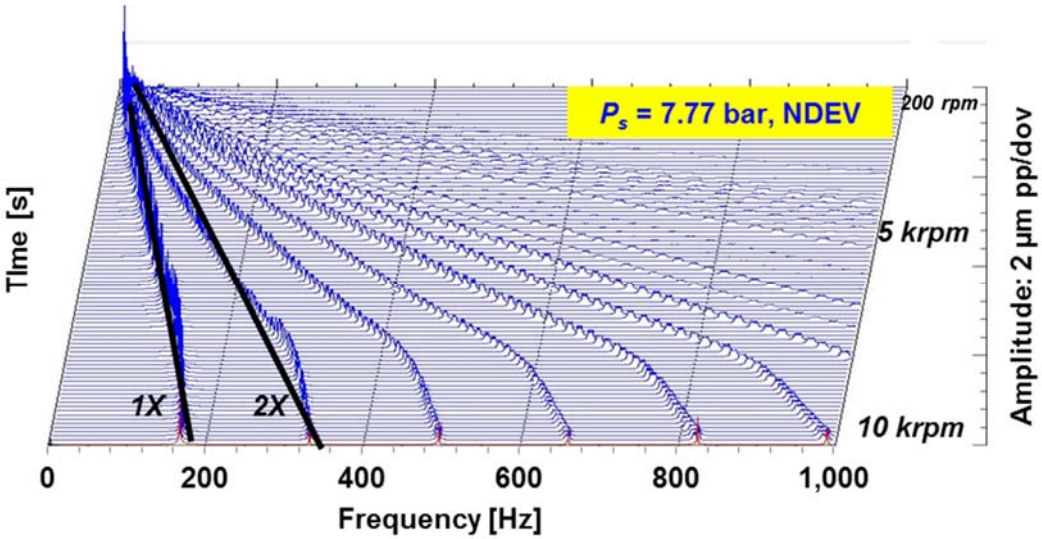

Figure 14. Waterfall plot of baseline coast down response at drive end, vertical plane (DEV). P_s = 7.77 bar, T_s = 21 °C.

In the following graphs, note that the depicted rotor motion shows the recorded amplitude and phase angle due to the inserted imbalance minus the recorded baseline response due to (any) remnant imbalance. At each supply pressure condition into the bearings, the baseline rotor motion is recorded with no added mass inserted in the end cap.

In the operating speed range from 0 to 10 krpm, the solid rotor can be regarded as rigid (see Appendix A). Preliminary rotordynamic tests were conducted with shaft speed to 10 krpm ($R_r \cdot \Omega_0$ =52 m/s) and with increasing mass imbalance. For a supply pressure of 7.77 bar, Figure 15 displays the amplitude of synchronous rotor response versus rotor speed recorded with the four displacement sensors. The added imbalance m_3 = 6.90 g.

Note that the rotor 1X amplitude steadily increases to reach and to traverse a critical speed at ~ 9 krpm, as also evidenced by the phase angles depicted in Figure 17. However, further operation with the same imbalance (m_3) and with the bearings supplied with a reduced pressure at 5.15 bar, led to the rotor experiencing a seizure in the DE bearing while attempting to traverse the first critical speed with a large amplitude of vibration. Fortunately, the flexible coupling as well as the limited motor torque prevented a catastrophic event, thus maintaining the integrity of the rotor as well as the bearings pads.

A short duration event (less than 3 s) with an increase in pad temperature of ~15 °C preceded the DE bearing seizure. At the time, there was no safety logic in place and the operators were unable to stop the rig. After the seizure, the pads in the DE bearing displayed visible wear marks. However, it is important to note that a simple smoothing process (with a shop towel and rubbing alcohol) restored the porous surfaces to a usable condition.

Despite the seizure event, after the simple restoration process, the porous bearing still float the rotor at a relatively low supply pressure of ~5 bar. To ensure safe operation (w/o bearing seizure), the remaining tests were conducted up to a maximum rotor speed of 8 krpm that avoids passage through the system first critical speed.

Figure 16 displays the amplitude rotor response to 6.90 g of added imbalance for a supply pressure of 7.77 bar. These results are recorded post seizure event. Comparing the responses presented in Figure 15 and Figure 16, the shaft motion at the NDE bearing behaves almost identically both before and after the seizure. However, the shaft motion at the DE bearing shows a slight reduction in amplitude at the highest speed, 8 krpm.

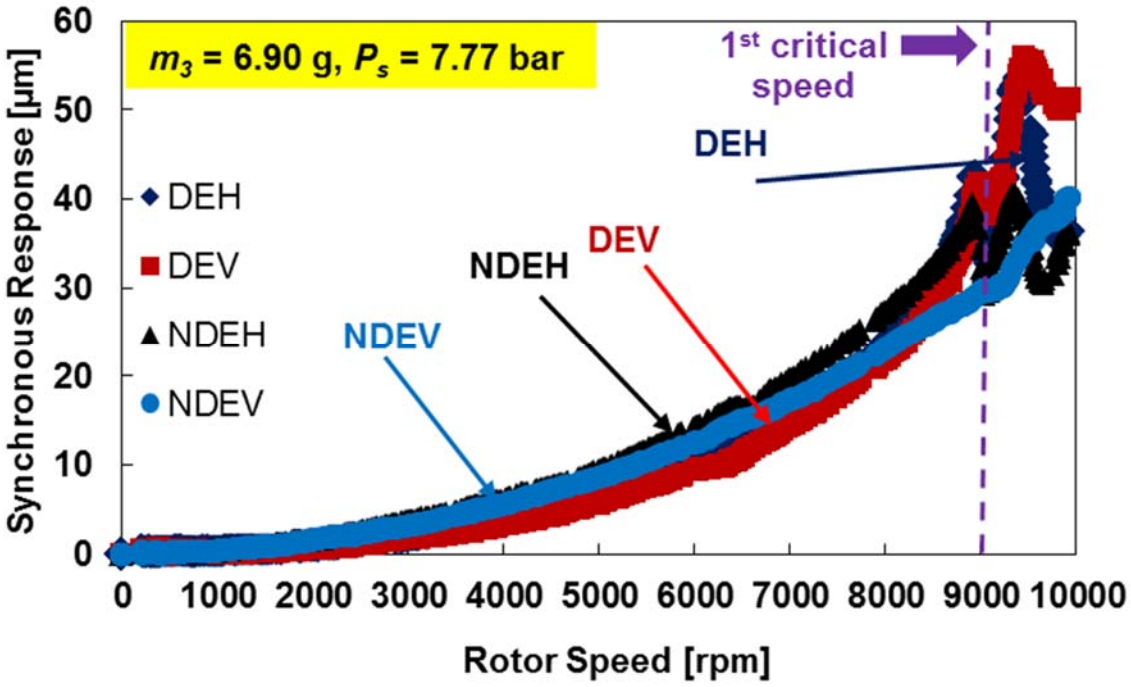

Figure 15. Amplitude of synchronous rotor response at DE and NDE bearings in horizontal and vertical directions. Added mass imbalance of 6.90 g. Bearings supplied with air at P_s = 7.77 bar. T_s = 21 °C.

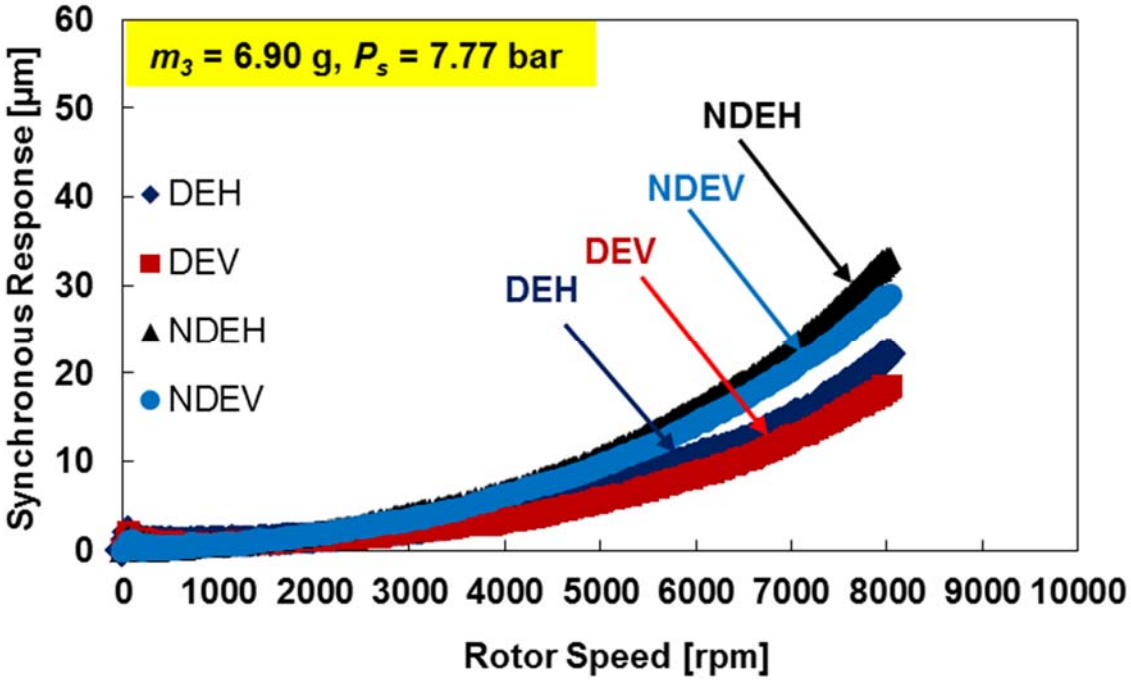

Figure 16. Amplitude of synchronous rotor response at DE and NDE bearings in horizontal and vertical directions after seizure event. Added mass imbalance of 6.90 g. Bearings supplied with air at P_s = 7.77 bar. T_s = 21 °C.

Figure 17 shows the phase angle versus rotor speed during the unbalance tests with added imbalance m_3 = 6.90 g, at DE bearing in horizontal direction. The phase angle under supply pressure of 7.77 and 6.53 bar are very close to each other sharing the same trend. Note that they both pass 90º at shaft speed rather close to 9 krpm, evidencing the first system critical speed.

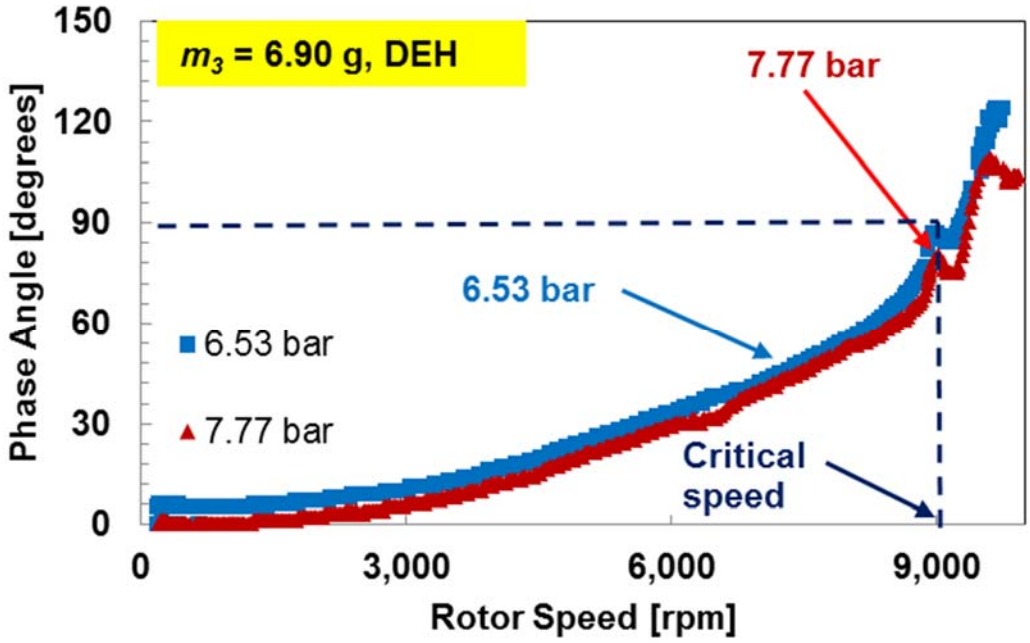

Figure 17. Phase angle of synchronous rotor motions for increasing supply pressure along horizontal plane. Drive end. Added mass imbalance m_3 = 6.90 g. T_s = 21 °C.

Figure 18 displays the phase angle difference for the rotor motions (horizontal or vertical) at the DE and NDE bearing locations. Note for example DEH refers to horizontal rotor motions recorded at the drive end. At a low rotational speed (less than 3 krpm) the rotor displacements at the DE and NDE locations are in phase. As the rotational speed increases and approaches the first critical speed, the differences in phase angle grow towards 180° thus indicating a conical mode of motion, as expected since the imbalance mass is added on one end of the rotor.

Figure 19 depicts the amplitude of rotor synchronous response versus rotor speed, prior to the seizure event, for operation with various added mass imbalances. The bearings have a supply pressure of 7.77 bar. As indicated, before the synchronous response peaks at 9 krpm, the rotor vibration amplitude increases almost proportionally with the mass imbalance, indicating a linear rotordynamic response of the system.

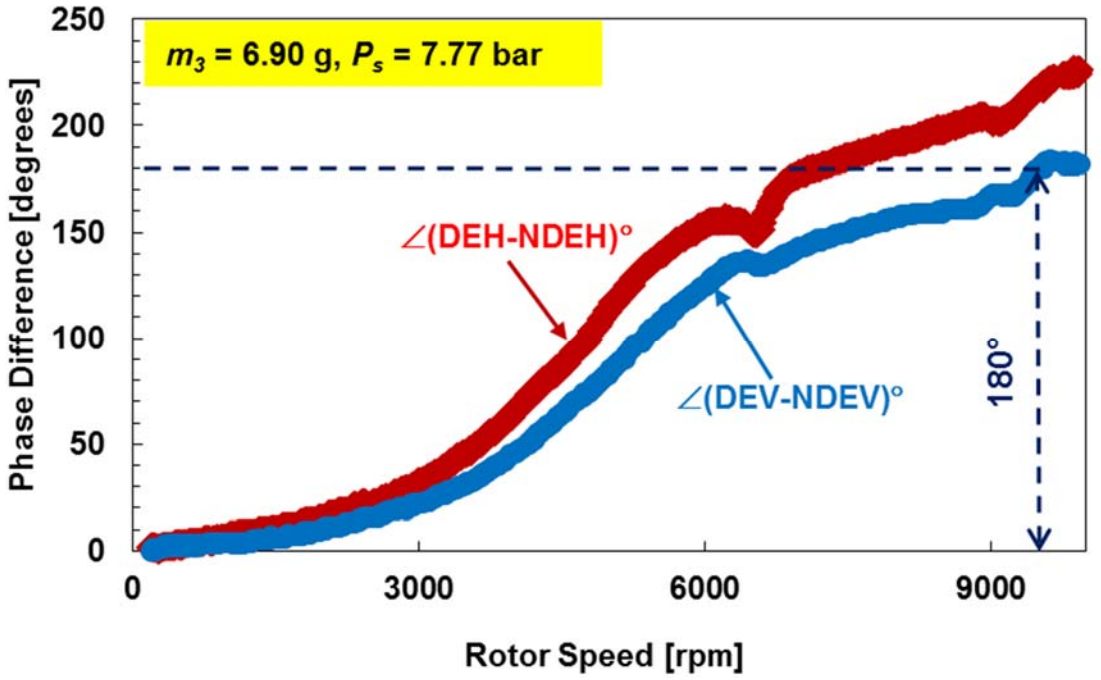

Figure 18. Difference in phase angle for synchronous rotor motions at DE and NDE bearings prior to seizure. Added mass imbalance of 6.90 g. Bearings supplied with air at P_s = 7.77 bar. T_s = 21 °C.

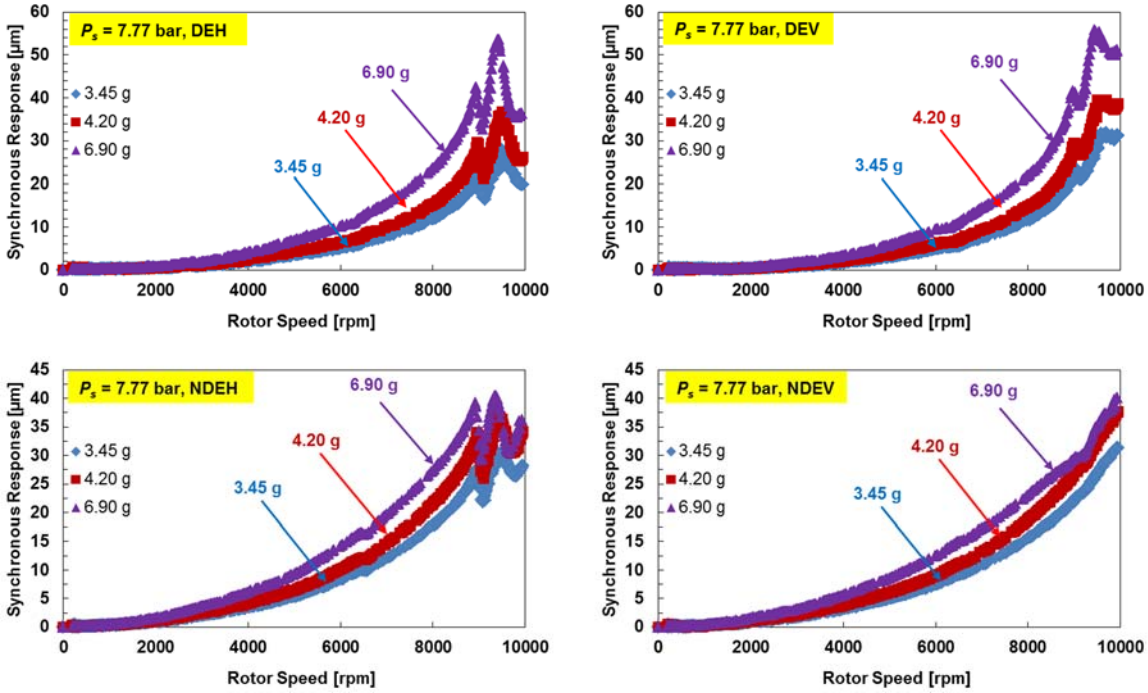

Figure 19. Amplitude of synchronous rotor response at DE and NDE bearings in horizontal and vertical directions. Added imbalance of 3.45, 4.20 and 6.90 g. Bearings supplied with air at P_s = 7.77 bar, T_s = 21 °C.

Since the synchronous rotor motions at the DE and NDE bearing locations display similar behavior, and the integrity of the DE bearing is compromised by the seizure, the analysis focuses on the rotor motions along the vertical direction and at the NDE bearing location.

Figure 20 displays the amplitude of rotor motion versus rotor speed for operation with the bearings at increasing supply pressure (5.84-7.77 bar) and with increasing levels of mass imbalance (3.45 - 6.90 g). Measurements show that increasing the supply pressure from 5.84 bar to 7.77 bar decreases the (largest) amplitude of motion at 8 krpm by just ~10% for each imbalance mass added. Most notably, increasing the imbalance mass from 3.45 g to 6.90 g increases the amplitude of motion by a factor of two.

Note that before the seizure event, the test rotor was able to float and spin nearly friction-free at a supply pressure as low as 3.77 bar (absolute). To ensure safety, the motor drives the test rotor up to 6 krpm with a supply pressure into bearings at P_s = 3.77 bar. Figure 21 presents the rotor synchronous response with increasing added imbalance, also indicating a linear increase in the synchronous response amplitude along with the added imbalance.

Scaling (normalizing) the rotor amplitude via mass imbalance ratios (λ) aids in assessing the linearity in response for the rotor-bearing system. Let

$$\lambda_1 = \frac{m_1}{m_2} = 0.82 \text{ and } \lambda_2 = \frac{m_1}{m_3} = 0.5 \tag{8}$$

where $m_{1\text{-}3}$ are listed in Table 3. Figure 22 displays the scaled amplitude of rotor motion at the NDE bearing. The bearings are supplied with air at 7.77 bar. The results show that the scaled responses are nearly identical, further evidencing that the rotor supported on the porous gas bearings behaves as a linear rotordynamic system.

Table 3 sums the maximum amplitude of rotor motion recorded. Increasing the supply pressure into the bearings does little to attenuate the amplitude of the synchronous rotor motions. This outcome at first appears surprising as an externally pressurized bearing (such as the current ones) should render a centering stiffness growing with the magnitude of supply pressure. However, the flow rate measurements (see Figure 7) already show the gas film has little influence on the pressure drop across the porous bearings.

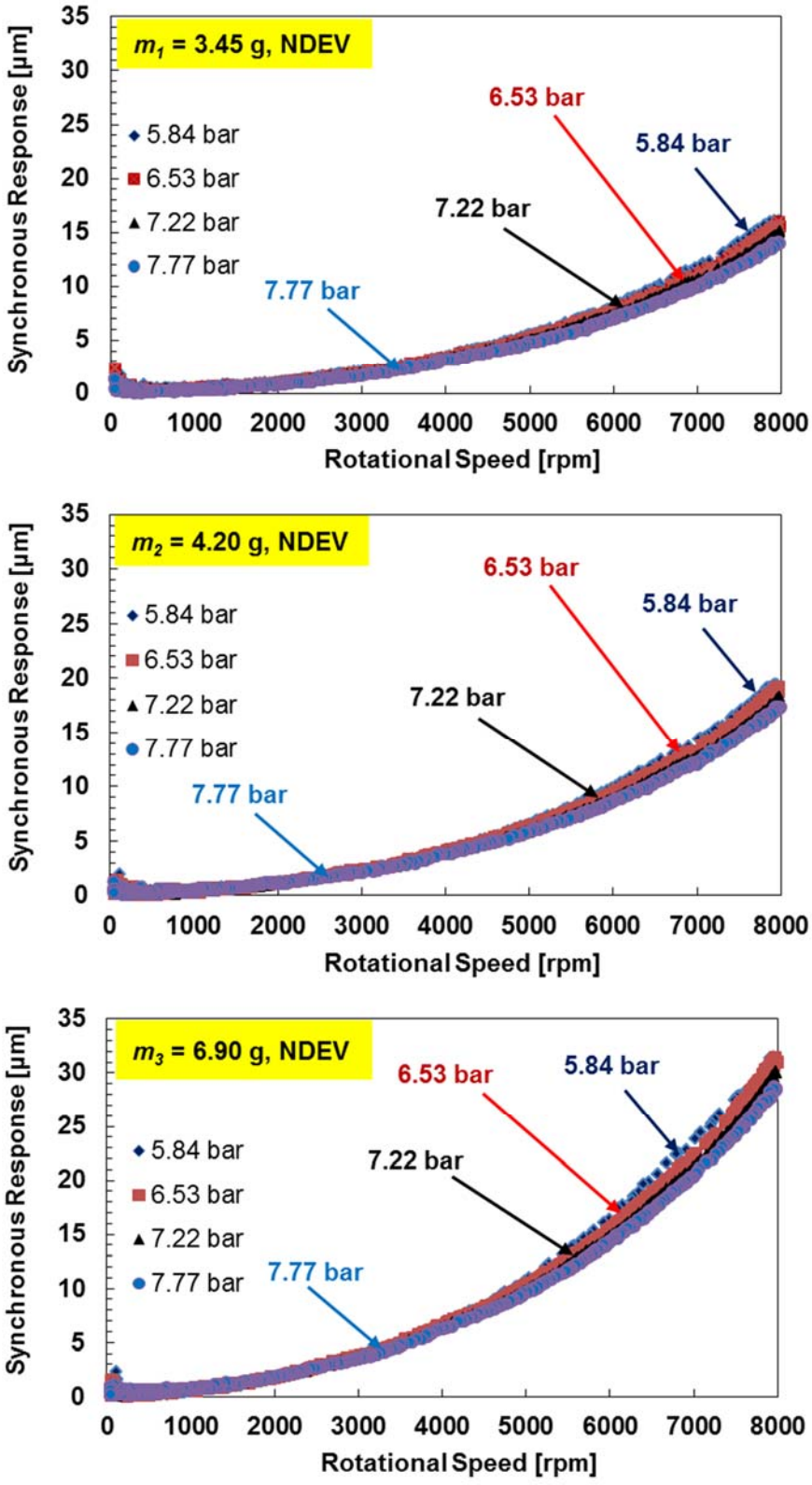

Figure 20. Synchronous response versus rotor speed in vertical direction at NDE bearing for added imbalance of 3.45 g, 4.20 g, and 6.90 g, respectively, with increasing supply pressure. T_s = 21 °C.

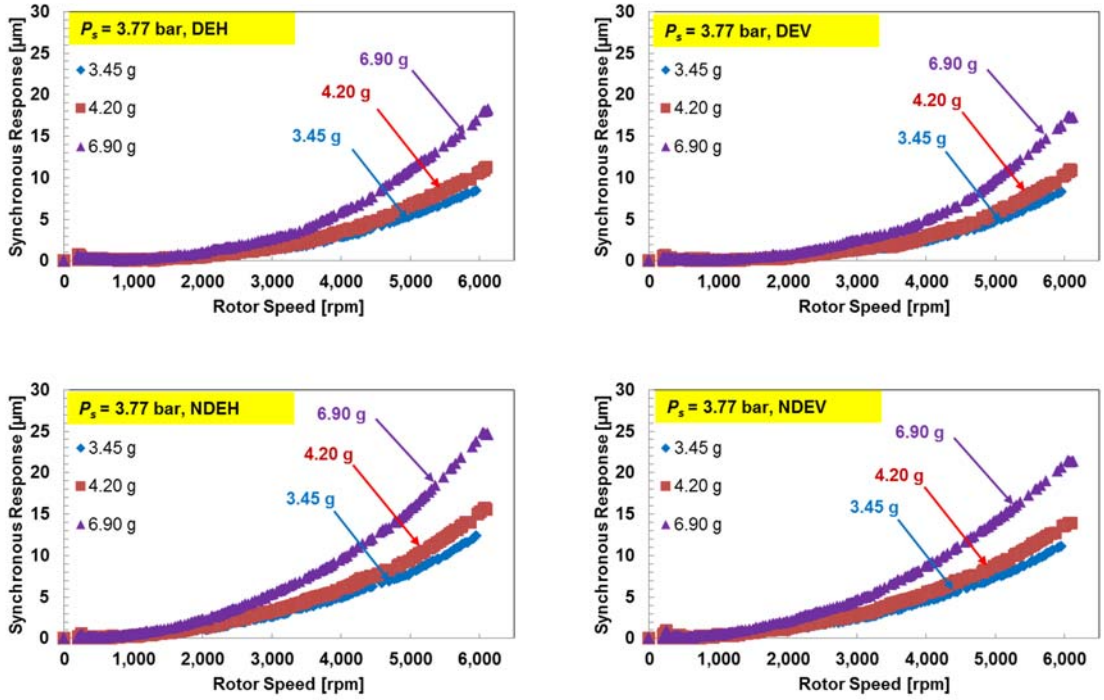

Figure 21. Amplitude of synchronous rotor response at DE and NDE bearings in horizontal and vertical directions. Added imbalance of 3.45, 4.20 and 6.90 g. Bearings supplied with air at P_s = 3.77 bar, T_s = 21 °C.

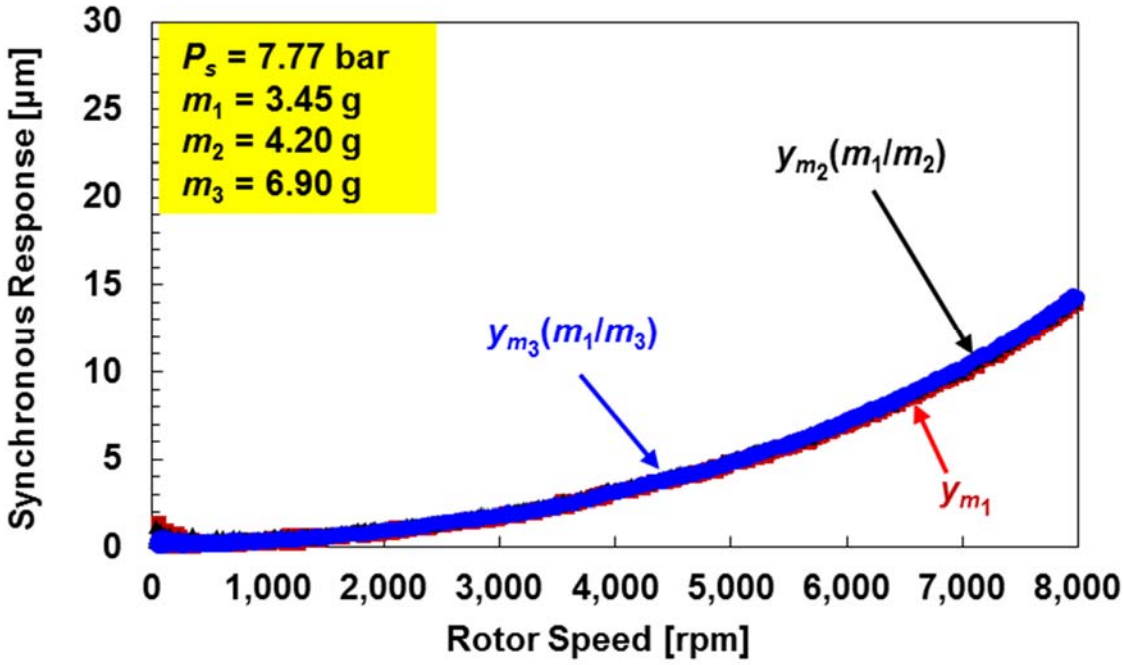

Figure 22. Scaled amplitude of synchronous rotor motion vs. rotor speed. Measurements along vertical direction at the NDE bearing location. P_s = 7.77 bar. Three imbalance masses m_1=3.45 g, m_2=4.20g and m_3=6.90g.

Table 3. Peak amplitude of rotor synchronous response at NDE bearing in vertical direction under varying operating conditions.

Supply Pressure P_s [bar, abs]	Added mass imbalance		
	m_1= 3.45 g	m_2= 4.20 g	m_3= 6.90 g
	Amplitude [μm]	Amplitude [μm]	Amplitude [μm]
3.77	11.0	14.0	21.5
5.84	15.9	19.4	31.5
6.53	15.8	19.1	31.3
7.22	15.1	18.3	30.2
7.77	14.1	17.7	29.0

STATIC LOAD TESTS

A hydrostatic (porous bearings) load mechanism applies a static force on the rotor. The load mechanism comprises a mounting base, two steel straps, one strain gauge load cell, one load bar, and four load pads. Figure 23 depicts the isometric and side views, and a free-body diagram (FBD) with the applied load and reaction force from the bearings. The load pads have the same dimensions as the bearing pads in both structure and material. Similar to the supporting bearing pads, pressurized air feeds into the load pads through an independent supply line and generates the static load to the test shaft.

Note that a significant pressure drop occurs through the porous layer of a load pad, hence the supply pressure into load pads is not directly applicable for the calculation of static load. The load cell measures the static load applied to the test rotor.

According to the free-body-diagram (FBD) shown in Figure 23 (b), the static equilibrium of the load forces are:

Force balance of rotor: $$F_{st} + W_r = F_{NDE} + F_{DE} \tag{9}$$

Moment balance rotor: $$F_{DE} \cdot L_4 + \frac{F_{st}}{2} \cdot L_6 = F_{NDE} \cdot L_7 + \frac{F_{st}}{2} \cdot (L_5 - L_6) \tag{10}$$

where, F_{st} is the static load applied to the test rotor and measured by the load cell, W_r is the rotor weight, F_{DE} and F_{NDE} are the reaction force from drive end and non-drive end bearings, respectively.

During the static load tests, the air supply pressure into the bearing pads is 6.53, 7.22 and 7.77 bar (absolute), respectively. Under each supply pressure, static load applied radially to the test shaft equals to 23 ~ 79 N, in the vertical direction.

Table 4 presents the calculated static load applied to the test rotor along vertical plane, as well as the estimated reaction load on the DE and NDE bearings, respectively.

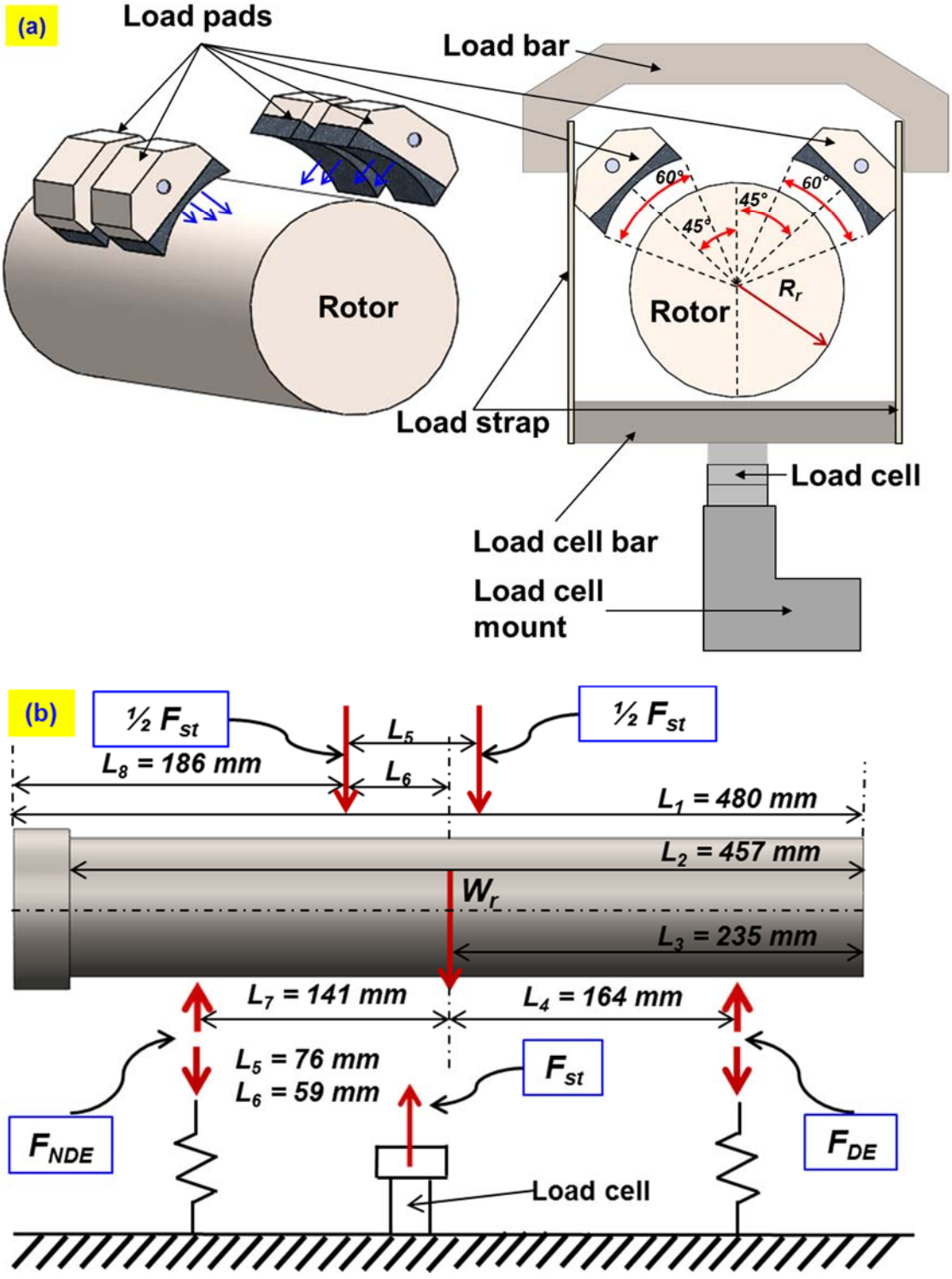

Figure 23. Hydrostatic loading mechanism: (a) Isometric and side views and (b) free-body diagram of applied load and reaction force from bearings.

Figure 24 depict the estimated direct stiffness coefficients of the DE bearing along the vertical direction (K_{yy} ~ 19.7 MN/m for P_s = 7.77 bar). The estimated stiffness coefficients are relatively insensitive to the static load applied to the test rotor. Further, increase in the supply pressure into bearings (6.53 to 7.77 bar) results in an increase in the direct stiffness coefficients. Note that the estimated direct stiffness from the static load tests at P_s = 7.77 bar is close to the value of K_{yy} estimated from impact tests in Appendix B (~20.4 MN/m).

Table 4. Static load applied to test rotor and estimated reaction load from bearings.

Static load	Reaction load from DE bearing		Reaction load from NDE bearing	
F_{st} [N]	F_{DE} [N]	$F_{DE}/(L_b \cdot D_r)$ [kPa]	F_{NDE} [N]	$F_{NDE}/(L_b \cdot D_r)$ [kPa]
0	132	18	153	21
23	141	19	167	23
32	145	20	173	24
42	148	20	179	24
51	152	21	184	25
60	155	21	190	26
70	159	22	195	27
79	163	22	201	28

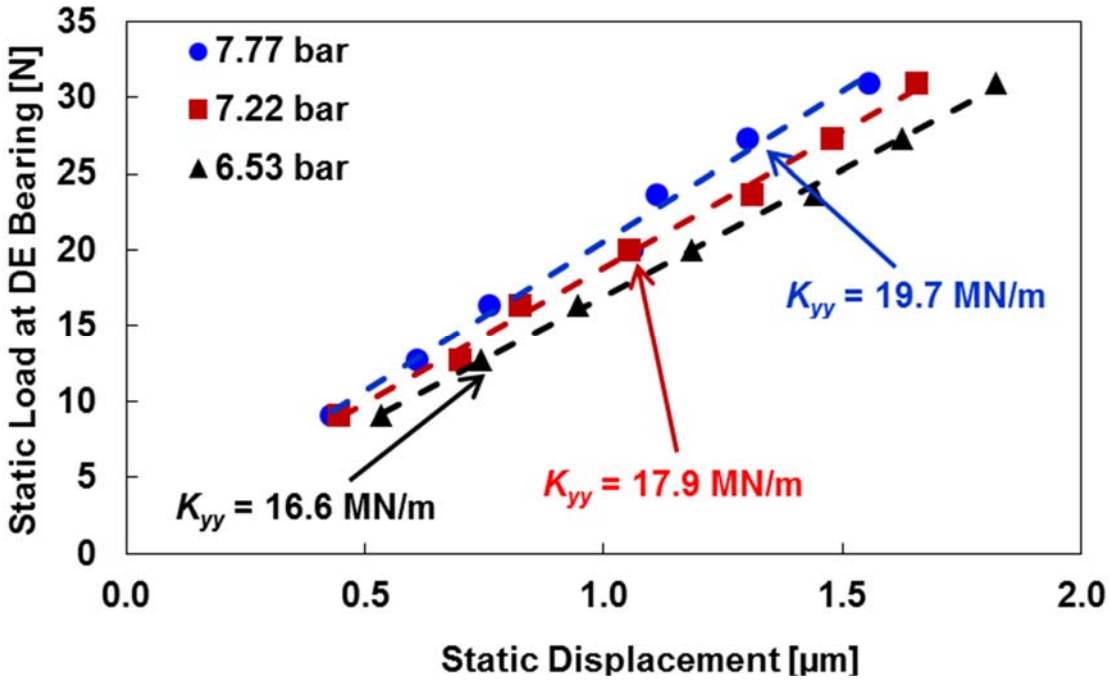

Figure 24. Estimated DE bearing direct stiffness K_{yy}. Supply pressure P_s= 6.53, 7.22 and 7.77 bar. T_s = 21 °C.

Table 5 presents the estimated shaft center displacement along the vertical directions, as well as the change in reaction load at the DE bearing (ΔF_{DE}) due to the static load, leading to an estimation of the direct stiffnessnes (K_{yy}) of DE bearing.

Table 5. Displacement and increase in reaction load at DE bearing due to static load applied to test rotor. Supply pressure into bearings at 7.77 bar, T_s = 21°C.

Static load on rotor	Increase in reaction load of DE bearing	Rotor displacement at DE bearing
F_{st} [N]	ΔF_{DE} [N]	Δy [μm]
23	13	0.61
32	16	0.76
42	20	1.06
51	24	1.11
60	27	1.30
70	31	1.56

VI. CONCLUSIONS

Experiments on a rotor-tilting pad porous gas bearing system are performed regarding flow rates, rotor speed coast down, and imbalance response. Two tilting pad carbon-graphite porous gas bearings support the test rotor, 29.12 kg and 100 mm in diameter. Each test bearing comprises five arcuate 60° pads with offset 50%.

Measurements indicate that the gas flow delivered into the porous bearings is proportional to the supply pressure ($P_s/P_a > 3.0$). The ratio of flow rate to pressure drop gives an estimation of the permeability coefficient (κ) at ~1.2 x 10^{-15} m^2, on the low end of known porous media for bearing materials. With the rotor installed, the supply pressure into the bearings to lift the rotor is ~3 bar (absolute). In this case, the mass flow rate to the bearings drops a little (max. 15%) thus indicating the operating air gap or film thickness between the pads and rotor is not small enough to restrict the supply of gas flow.

Rotor speed coast down tests from a top speed of 8 krpm (surface speed = 42 m/s) show a deceleration driven mainly by the viscous drag in the porous bearings and lasting at least two full minutes to come to rest. Measurements identify the rotational drag coefficient that leads to a low friction factor (f), as small as 0.03 for operation with the bearings supplied with pressure at 5.84 bar. With a supply pressure of 7.77 bar, the friction factor from the bearings decreases to 0.019, a

nearly friction free operation. From the top speed, the rotor requires a minimum of two minutes to come to rest, indicating very little friction.

Measurements of the rotor dynamic response were conducted with various imbalance masses and for operation with an increasing supply pressure into the bearings. The rotor-bearing system crosses a (lightly damped) critical speed at about 9 krpm. Alas, when operating near 10 krpm, seizure of the rotor occurred while exercising the largest imbalance and the bearings fed with the lowest supply pressure (5.15 bar). Fortunately, the damage to the bearings and rotor was minimal. A simple cleaning process restored the bearings to a working condition. To avoid further seizure events, further rotordynamic tests were conducted only to a top speed of 8 krpm (surface speed = 42 m/s)

The rotordynamic measurements show the shaft motion is mainly synchronous and with amplitude steadily increasing with rotor speed as it approaches the critical speed. Since the imbalance masses are located at one rotor end, the rotor motion is mainly conical. Most importantly, however, is to realize the amplitude of rotor response is proportional to the imbalance mass; hence demonstrating the rotor-bearing system is linear. This assertion cannot be generalized to rotordynamic performance with other types of gas bearings, foil bearings for example.

Regarding rotor synchronous response due to imbalance, predictions obtained with an in-house rotordynamics software [12] demonstrate a reasonable agreement with the recorded response for rotor motions at DE bearing. Note that the predictions obtained from the software relies on simulating the support bearings with estimated force coefficients from a set of impact tests on the test rotor (floating, no rotation) with varying supply pressure.

A well-developed computational physics model accounting for flow characteristics related properties of CG-PGBs, i.e., permeability, friction factor and air film thickness, promises accurate and reliable predictions on the rotordynamic performance of tilting pad porous gas bearings.

REFERENCES

[1] Valco, M. J., DellaCorte, C., 2002, "Emerging Oil-Free Turbomachinery Technology for Military Propulsion and Power Applications," *Proc. 23rd U.S. Army Science Conference*, Fort Lauderdale, FL.

[2] San Andrés, L., 2014, *Modern Lubrication Theory,* "Gas Lubrication," Notes 15, Texas A & M University Digital Libraries, http://repository.tamu.edu/handle/1969.1/93197 [03/25/2016]

[3] Sneck, H. J., 1968, "A Survey of Gas-Lubricated Porous Bearings," ASME J. Lubric. Technol., **90**, 804-809.

[4] Heller, S., Shapiro, W., Decker, O., 1971, "A Porous Hydrostatic Gas Bearing for Use in Miniature Turbomachinery," ASLE Trans., **14**, pp. 144-155.

[5] Majumdar, B. C., 1976, "Gas-Lubricated Porous Bearings: A Bibliography", Wear, **36**, pp. 269-273.

[6] Montgomery, A. G., Sterry, F., 1955, "A Simple Air Bearing Rotor for Very High Rotating Speeds," AERE ED/ R 1671, Harwell, Berkshire, England.

[7] Sneck, H., and Yen, K., 1964, "The Externally Pressurized, Porous Wall, Gas-Lubricated Journal Bearing," ASLE Trans., **7**(3), pp. 288-298.

[8] Sneck, H. J., and Elwell, R., 1965, "The Externally Pressurized, Porous Wall, Gas-Lubricated Journal Bearing. II," ASLE Trans., **8**(4), pp. 339-345.

[9] Sneck, H., and Yen, K., 1967, "The Externally Pressurized, Porous Wall, Gas-Lubricated Journal Bearing-III," ASLE Trans., **10**(3), pp. 339-347.

[10] Castelli, V. P., 1979, "Experimental and Theoretical Analysis of the Gas-Lubricated Porous Rotating Journal Bearing," ASLE Trans., **22**(4), pp. 382-388.

[11] San Andrés, L., Jeung, S.-H., Rohmer, M., Devitt, D., 2015 "Experimental Assessment of Drag and Rotordynamic Response for A Porous Type Gas Bearing," STLE Annual Meeting, Dallas, TX May 17-21.

[12] XLTRC^2, 2002, Computational Rotordynamics Software Suite, *Turbomachinery Laboratory, Texas A&M University.*

[13] San Andrés, L., Cable, A. T., Zheng, Y., De Santiago, O., Devitt, D., 2016, "Assessment of Porous Type Gas Bearings: Measurements of Bearing Performance and Rotor Vibrations," ASME

paper GT2016-57876, *Proceedings of the 61st ASME Turbo Exp*, Seoul, June 13 – 17 (to be published).

[14] Belforte, G., Raparelli, T., Viktorov, V., Trivella, A., 2007, "Permeability and Inertial Coefficients of Porous Media for Air Bearing Feeding Systems," ASME J. Trib., **129**, pp. 705-711.

[15] Raymond, M.S., Kasarda, M.E.F. and Allaire, P.E., 2008, "Windage Power Loss Modeling of a Smooth Rotor Supported by Homopolar Active Magnetic Bearings," ASME J. Trib., **130**, pp. 1-8.

[16] Miyatake, M., Yoshimoto, S. and Sato, J., 2005, "Whirling Instability of a Rotor Supported by Aerostatic Porous Journal Bearings with a Surface-Restricted Layer," Proc. IMechE, J. Eng. Tribol., **220**, pp. 1-9.

[17] De Santiago, O., 2002, "Identification of Bearing Supports' Force Coefficients from Rotor Responses Due to Imbalances and Impact Loads," Ph.D. Thesis, Mechanical Engineering, Texas A&M University, College Station, TX.

[18] ISO 1940-1, 2003, "Mechanical Vibration-Balance Quality Requirements for Rotors in a Constant (Rigid) State – Part 1: Specification and Verification of Balance Tolerances."

APPENDIX A. IMPACT TESTS TO IDENTIFY THE ROTOR FREE-FREE MODE SHAPES AND NATURAL FREQUENCIES [12]

Prior to installing the rotor on the air bearing supports, a free-free modal impact test characterizes the rotor natural frequencies and associated mode shapes. The rotor natural frequencies are 1,888 Hz and 4,488 Hz, respectively, well beyond the operating speed range up to 10 krpm (0~167 Hz). Hence, for practical purposes, the rotor is rigid while testing.

Table A.1 summarizes the measured and predicted inertia properties of the rotor and its elastic natural frequencies. Figure A.1 displays the rotor first and second elastic free-free modes of vibration. Predictions obtained with an in-house rotordynamics software match well with the measurements.

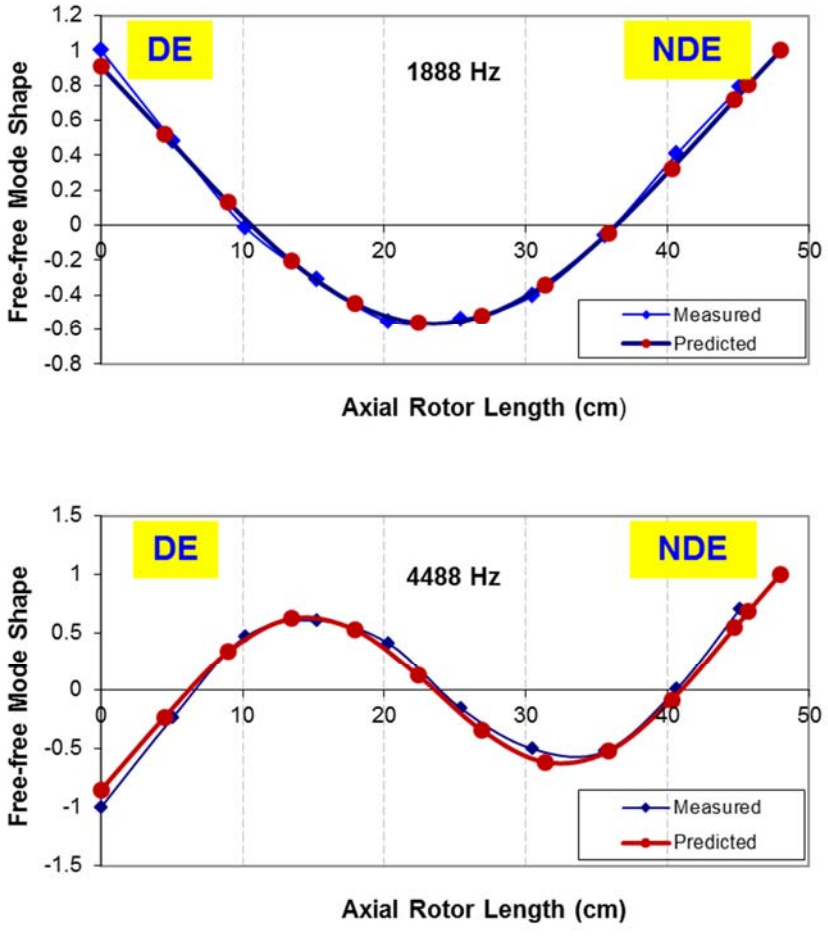

Figure A.1 Measured and predicted free-free mode shapes for the test rotor.

Table A.1 Physical and predicted rotor mass properties.

Parameter	Measured	Predicted	Difference
Mass [kg]	29.12	29.18	0.2 %
Center of gravity from drive end [cm]	23.47	23.45	0.1 %
I_p [kg.m^2]	0.0359	0.0373	3.9 %
I_t [kg.m^2]	0.5565	0.5544	0.4 %
First natural frequency [Hz]	1,888	1,881	0.4 %
Second natural frequency [Hz]	4,488	4,501	0.3 %

APPENDIX B. PREDICTION OF IMBALANCE RESPONSE [12]

With compressed air supplied into the DE and NDE bearings, a set of impact tests on the rotor (floating with no rotation) serve to identify the bearings' direct stiffness (K_{xx}, K_{yy}) and direct damping (C_{xx}, C_{yy}) coefficients. The location for the delivery of impact is at the NDE end cap, with corresponding acceleration response recorded (average out of 16 impacts). For the impact tests, the supply pressure into bearings varies as P_s = 3.77, 6.53, and 7.77 bar, respectively.

Numerical analysis yields the equivalent stiffness and damping coefficients of the rotor-bearing system at different supply pressure (P_s), by curve fitting the experimental dynamic accelerance functions (acceleration over force) recorded.

Figure B. 1 shows the spectrum of applied force recorded during an impact test with bearings supplied with pressure P_s = 7.77 bar. Figure B. 2 presents the test derived accelerance function and the corresponding curve fitting over the frequency range (0 – 640 Hz) for supply pressure equal to P_s = 7.77 bar. The peak of the acclerance indicates a system natural frequency close to 150 Hz. Figure B. 3 depicts the coherence function corresponding to the measured accelerance at P_s = 7.77 bar. The measurements show relatively good coherences throughout the frequency range 0 - 640 Hz.

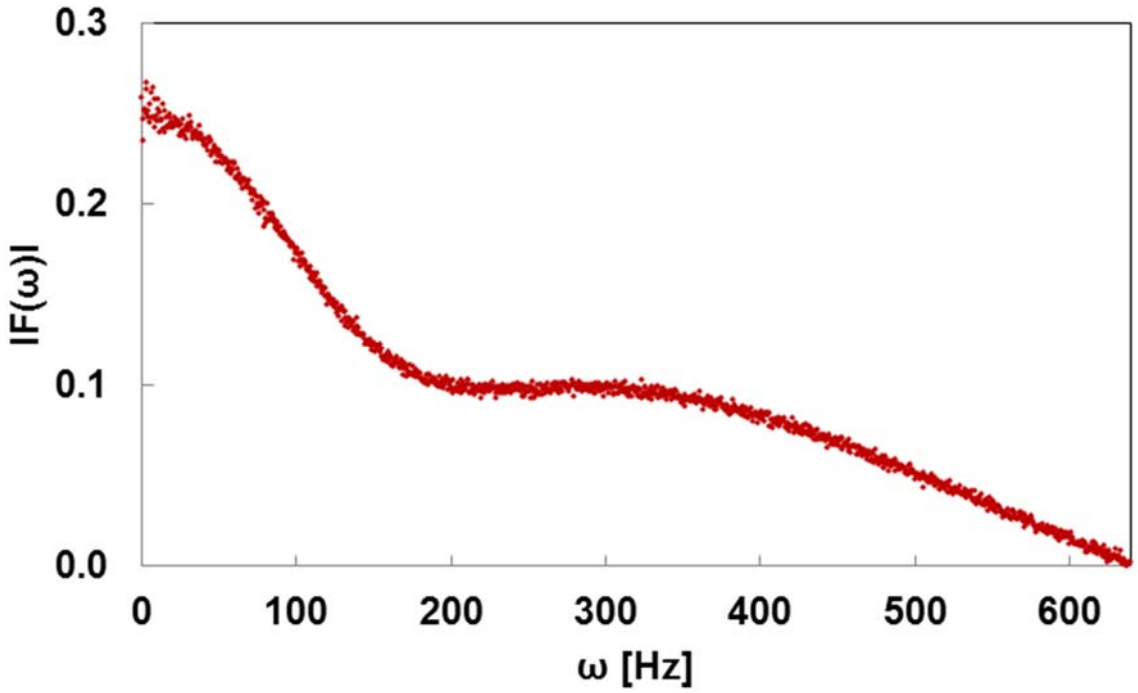

Figure B. 1 Force spectrum of an impact along vertical direction. P_s = 7.77 bar, T_s = 21 °C.

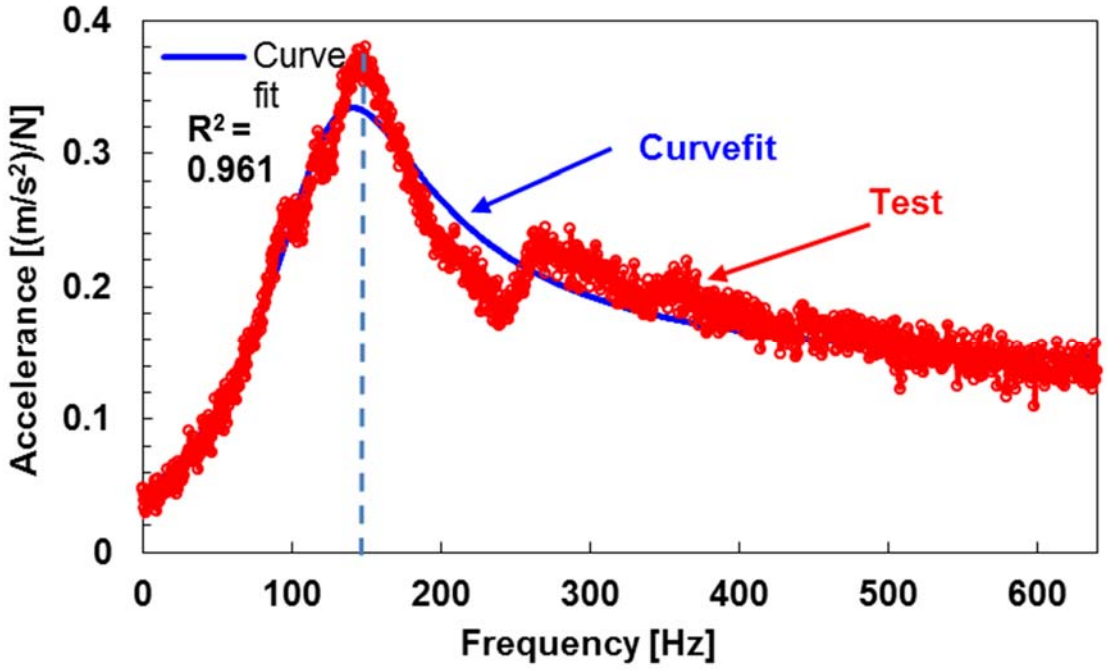

Figure B. 2 Transfer function (acceleration/force) of an impact along vertical direction. P_s = 7.77 bar, T_s = 21 °C.

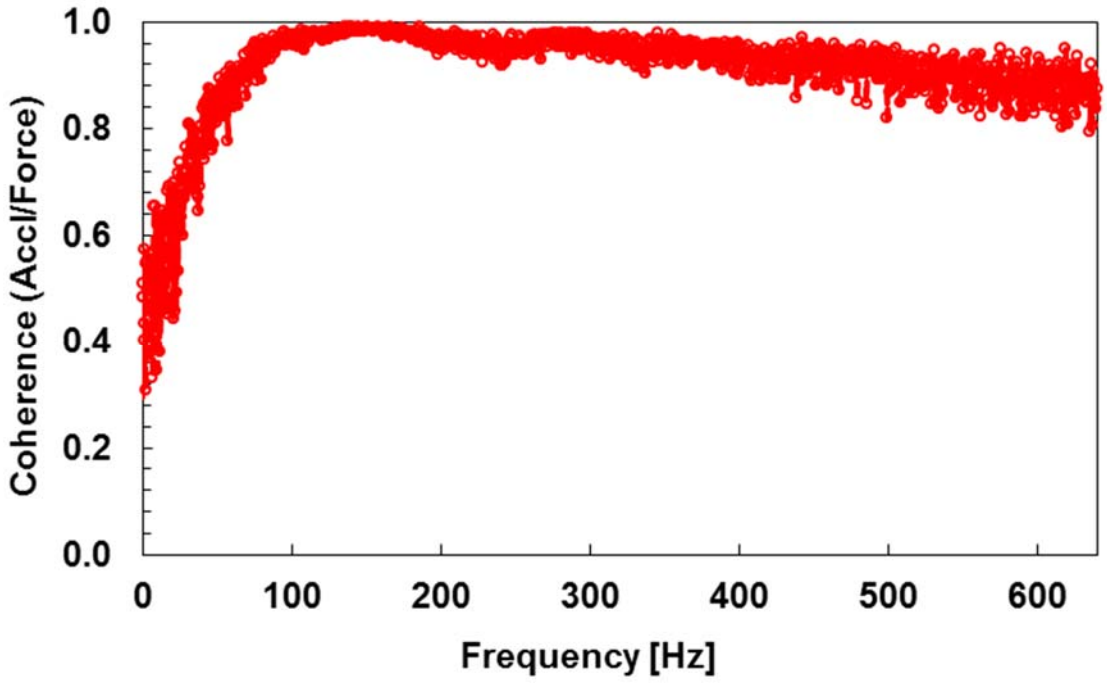

Figure B. 3 Coherence between the acceleration and force. P_s = 7.77 bar, T_s = 21 °C.

Force coefficients identified from the curve fitting, for bearings supplied with P_s = 7.77 bar (absolute), for instance, the estimated bearing direct stiffness coefficients are K_{xx} = 17.4 MN/m and K_{yy} = 20.3 MN/m, respectively, while the direct damping coefficients are C_{xx} = 5.6 kN·s/m and C_{yy} = 4.9 kN·s/m.

Following graphs present predictions from a finite element (FE) structural model regarding the rotor's response to added imbalance, simulating the support bearings with the above estimated force coefficients. Figure B. 4 shows the predicted undamped critical speed map allowing for a rough prediction of the stiffness of the rotor-bearing system. Figure B. 5 presents the damped critical speed map, indicating a first critical speed at 9 krpm for synchronous response.

Figure B. 6 presents the comparison between test and predicted response at P_s = 3.77 bar, with added imbalance of m_1 = 3.45 g, m_2 = 4.20 g and m_3 = 6.90 g, respectively. As depicted, the predictions at DE bearing generally agree well with the test results from null rotor speed to around 4000 rpm, beyond which discrepancies develop. As for rotor response at FE bearing, the comparison establishes a good correlation between predictions and test results for the whole rotor speed range. Note that a comprehensive predicting model for the porous gas bearing is not available at this moment; hence, full rotordynamic analysis is not obtainable.

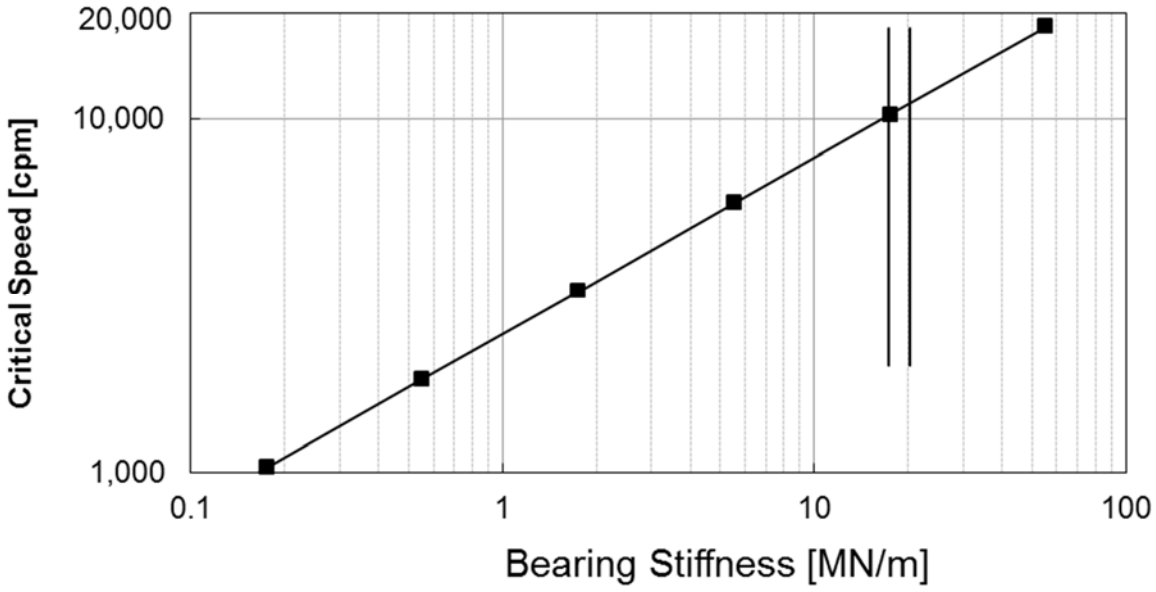

Figure B. 4 Undamped critical speed map for test rotor-bearing system.

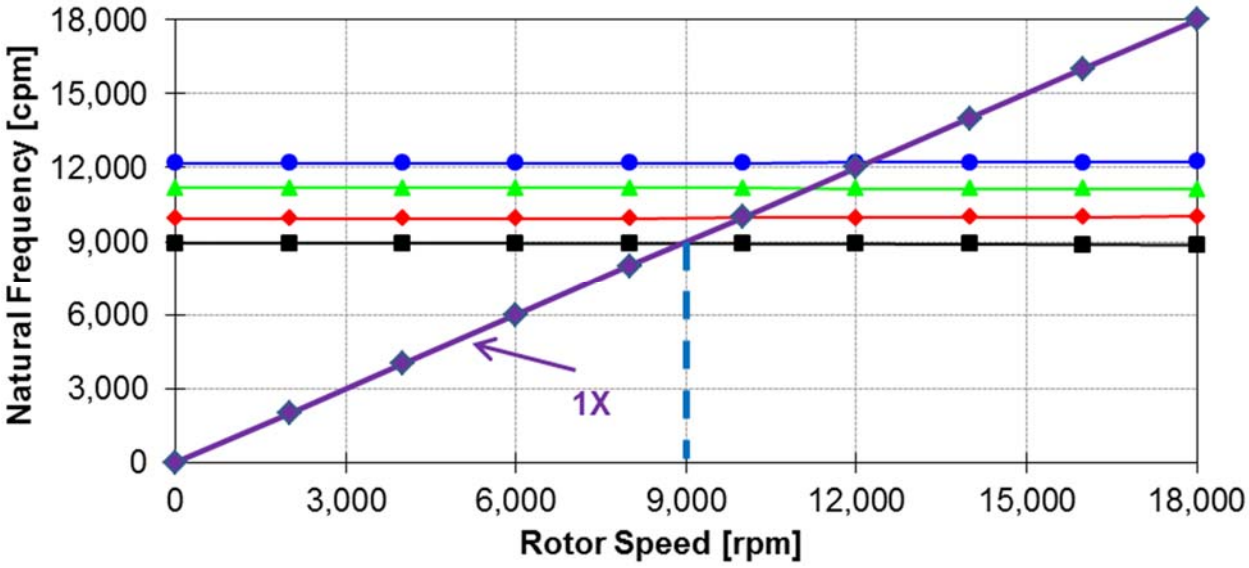

Figure B. 5 Damped critical speed map for test rotor-bearing system.

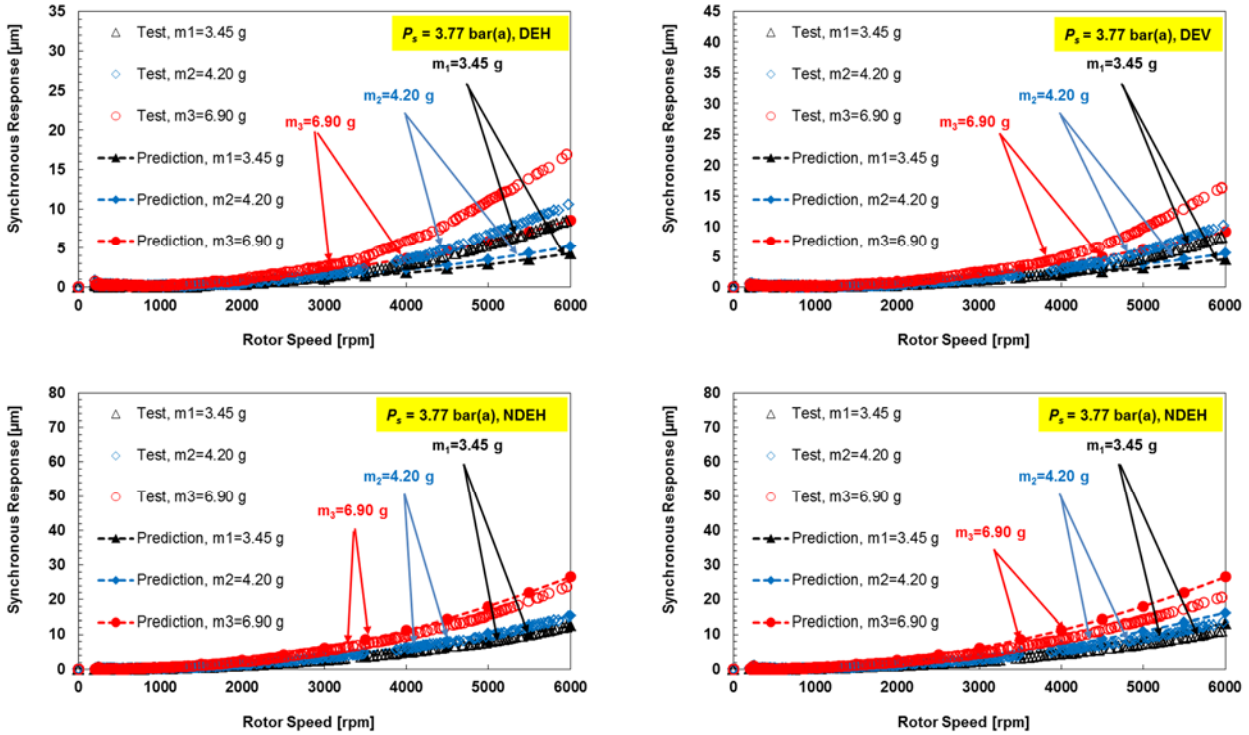

Figure B. 6 Comparison of synchronous rotor responses between test results and predictions. DE and NDE bearings in horizontal and vertical directions. Added imbalance of 3.45, 4.20 and 6.90 g. Ps =3.77 bar (absolute).